

A star formation study of the ATLAS^{3D} early-type galaxies with the AKARI all-sky survey

T. Kokusho¹, H. Kaneda¹, M. Bureau², T. Suzuki¹, K. Murata¹, A. Kondo¹, and M. Yamagishi³

¹ Graduate School of Science, Nagoya University, Chikusa-ku, Nagoya 464-8602, Japan
e-mail: kokusho@u.phys.nagoya-u.ac.jp

² Sub-department of Astrophysics, Department of Physics, University of Oxford, Denys Wilkinson Building, Keble Road, Oxford OX1 3RH, UK

³ Institute of Space and Astronautical Science, Japan Aerospace Exploration Agency, Chuo-ku, Sagami-hara 252-5210, Japan

October 17, 2018

ABSTRACT

Context. The star formation properties of early-type galaxies (ETGs) are currently the subject of considerable interest, particularly whether they differ from those of gas-rich spirals.

Aims. We perform a systematic study of star formation in a large sample of local ETGs using polycyclic aromatic hydrocarbon (PAH) and dust emission, focusing on the galaxies' star formation rates (SFRs) and star formation efficiencies (SFEs).

Methods. Our sample is composed of the 260 ETGs from the ATLAS^{3D} survey, from which we use the cold gas measurements (H I and CO). The SFRs are estimated from stellar, PAH and dust fits to spectral energy distributions created from new AKARI measurements and literature data from WISE and 2MASS.

Results. The mid-infrared luminosities of non-CO-detected galaxies are well correlated with their stellar luminosities, showing that they trace (circum)stellar dust emission. CO-detected galaxies show an excess above these correlations, uncorrelated with their stellar luminosities, indicating that they likely contain PAHs and dust of interstellar origin. PAH and dust luminosities of CO-detected galaxies show tight correlations with their molecular gas masses, and the derived current SFRs are typically $0.01 - 1 M_{\odot} \text{ yr}^{-1}$. These SFRs systematically decrease with stellar age at fixed stellar mass, while they correlate nearly linearly with stellar mass at fixed age. The majority of local ETGs follow the same star-formation law as local star-forming galaxies, and their current SFEs do not depend on either stellar mass or age.

Conclusions. Our results clearly indicate that molecular gas is fueling current star formation in local ETGs, that appear to acquire this gas via mechanisms regulated primarily by stellar mass. The current SFEs of local ETGs are similar to those of local star-forming galaxies, indicating that their low SFRs are likely due to smaller cold gas fractions rather than a suppression of star formation.

Key words. Galaxies: elliptical and lenticular, cD – Galaxies: star formation – Galaxies: ISM – Galaxies: photometry – (ISM:) dust, extinction – Infrared: galaxies

1. Introduction

Stellar population studies of local early-type galaxies (ETGs; ellipticals and lenticulars) show that they are dominated by old stars and reside in the so-called red sequence of the optical colour-magnitude diagram. This suggests that they ceased to form stars at an early stage of their evolution (e.g., Cowie et al. 1996; Thomas et al. 2010), and thus represent the end point of galaxy evolution.

The interstellar space of ETGs is generally filled with hot X-ray gas (e.g., Forman et al. 1985), that can heat and destroy any cold interstellar medium (ISM), the fuel for star formation. Nevertheless, atomic gas, molecular gas and dust have all been detected in a significant fraction of ETGs (e.g., Knapp et al. 1985; Wardle & Knapp 1986; Knapp et al. 1989; Knapp & Rupen 1996), and evidence for the presence of such cold gas and dust in ETGs has grown for the last two decades through both radio and infrared (IR) observations. In particular, Young et al. (2011) carried out a molecular gas survey of the 260 ETGs in the ATLAS^{3D} sample (Cappellari et al. 2011), that aimed to reveal the formation and evolutionary processes of nearby ETGs. With a high detection rate of 22%, they con-

firmed that molecular gas is prevalent in ETGs, suggesting that some ETGs may still be able to form new stars. Far-infrared (FIR) emission from cold dust in ETGs was systematically investigated first with the Infrared Astronomical Satellite (IRAS; Knapp et al. 1989). More recent observations with satellites such as the Infrared Space Observatory (ISO), Spitzer, AKARI and Herschel also detected dust of both circumstellar and interstellar origin in many ETGs (e.g., Temi et al. 2003; Kaneda et al. 2011; Smith et al. 2012). Polycyclic aromatic hydrocarbons (PAHs), that are destroyed by X-rays much more easily than dust, are also detected in some ETGs (e.g., Kaneda et al. 2005, 2008; Rampazzo et al. 2013). As PAHs are considered a star formation tracer, their presence in ETGs again suggests that star formation is ongoing. Indeed, PAHs are excited and ionised by far-ultraviolet (FUV) light from young stars, producing strong features primarily at wavelengths of 6.2, 7.7 and 8.6 μm , while they are destroyed by hard UV and X-ray radiation from active galactic nuclei (AGN; e.g., Peeters et al. 2004).

Utilizing PAH emission observed with Spitzer, Shapiro et al. (2010) investigated the star formation properties of the 48 ETGs in the SAURON sample (de Zeeuw et al. 2002), and argued that ETGs are forming stars with surface densities and efficiencies

similar to those of spiral galaxies. They also suggested that star formation in ETGs proceeds in at least two different modes (widespread and circumnuclear), that may reflect different evolutionary paths. With PAH and mid-infrared emission (MIR), Crocker et al. (2011) calculated the current star formation rates (SFRs) of the SAURON ETGs, and suggested that they form stars less efficiently than spiral galaxies. Using both numerical simulations and observational results, Martig et al. (2013) similarly argued that ETGs have lower star formation efficiencies (SFEs; defined as the SFR per unit cold gas mass M_{gas}) than spiral galaxies, likely due to the increased stability of discs embedded in spheroids (morphological quenching). The same trend is reported in the ATLAS^{3D} sample using SFRs estimated from MIR and FUV light (Davis et al. 2014). It has also been suggested that AGN and galaxy mergers can respectively heat (and expel) and strip away the cold ISM of ETGs, thus suppressing star formation (i.e., lowering the SFE; see, e.g., Schawinski et al. 2006; Nesvadba et al. 2011; Alatalo et al. 2015; Guillard et al. 2015; Lanz et al. 2016). It is therefore likely that while ETGs have a substantial cold ISM and are forming stars, their SFE is reduced with respect to that of spiral galaxies, due to a number of properties and mechanisms particular to them.

In a different vein, the sources of the cold ISM in ETGs are themselves a matter of debate. As mentioned above, the stellar populations of ETGs are uniformly old, indicating that the original cold gas reservoirs that led to galaxy formation have already been consumed (e.g., Bower et al. 1992). In addition, old stars do not efficiently produce dust, and ETGs are filled with hot X-ray gas, that can destroy dust through sputtering (e.g., Draine & Salpeter 1979). Yet Goudfrooij & de Jong (1995) clearly demonstrated that ellipticals contain more dust than that expected from the balance between production via stellar mass loss (e.g., Faber & Gallagher 1976) and destruction via X-ray sputtering. Galaxy mergers are therefore frequently invoked as a possible mechanism to supply cold gas and dust to ETGs. For example, Davis et al. (2011) studied the kinematics of stars, ionised gas and molecular gas in ETGs and, due to the pervasiveness of kinematic misalignments between stars and gas, suggested that the majority of them may obtain cold gas from external sources. Internal sources are however also proposed by several authors. For example, based on the spatial distribution of dust and X-ray gas, it has been suggested that intermittent buoyant outflows from low-luminosity AGN can replenish dust in ellipticals (e.g., Temi et al. 2007; Kaneda et al. 2011). Continuous dust production by old stars and dust growth in the ISM are other potential channels for dust production in ETGs (Martini et al. 2013; Hirashita et al. 2015).

Depending on how ETGs obtain their gas and dust, star formation may well proceed differently. A systematic study of the cold ISM properties of a large sample of ETGs, coupled with constraints on their star formation activity, is thus essential to properly understand ETG evolution. Here, we systematically investigate the star formation properties of the ATLAS^{3D} ETGs using PAH and dust emission measured from the AKARI all-sky survey, combined with Wide-field Infrared Survey Explorer (WISE) and Two Micron All Sky Survey (2MASS) archival data, and atomic and molecular gas data from ATLAS^{3D}. We detail our measurements in Sect. 2 and present the main results in Sect. 3. The star formation properties of ETGs are discussed in Sect. 4 and we summarise our results in Sect. 5.

2. Sample and Data

2.1. ATLAS^{3D} survey

The goal of the ATLAS^{3D} project was to conduct a comprehensive study of a complete, volume-limited sample of 260 morphologically-selected local ETGs ($M_K < -21.5$ and $D < 42$ Mpc; Cappellari et al. 2011). A diverse range of observations and simulations was performed, at its core optical integral-field spectroscopic observations with the SAURON instrument (Bacon et al. 2001), yielding detailed information on the stellar kinematics (Krajnović et al. 2011; Emsellem et al. 2011; Krajnović et al. 2013a,b) and populations (Cappellari et al. 2012; Scott et al. 2013; McDermid et al. 2014, 2015). In addition to single-dish molecular gas surveys (Combes et al. 2007; Young et al. 2011), both H_I and CO interferometric observations were obtained (Young et al. 2008; Crocker et al. 2011; Serra et al. 2012; Alatalo et al. 2013). The morphology and kinematics of the molecular gas are characterised in Davis et al. (2013), while its physical conditions are discussed in Crocker et al. (2012) and Bayet et al. (2013).

2.2. AKARI all-sky survey

The new IR fluxes presented here were obtained from the AKARI satellite (Murakami et al. 2007) all-sky surveys in the MIR (central wavelengths 9 and 18 μm ; Onaka et al. 2007) and FIR (65, 90 and 140 μm ; Kawada et al. 2007). For the MIR 9 and 18 μm bands, the total galaxy flux densities were obtained through aperture photometry as follows. First, we applied a spatial filtering of 1.3 arcmin⁻¹ to each galaxy image, to remove periodic noise. Second, we performed aperture photometry on the all-sky diffuse maps (Doi et al. 2015; Ishihara et al., in preparation), within a circular aperture of radius $R_{\text{aper}} = \sqrt{(2R_e)^2 + (1.5D_{\text{PSF}})^2}$, where R_e is the effective radius of each galaxy in the optical B band (Cappellari et al. 2011) and D_{PSF} is the full width at half maximum of the point spread function (PSF) of the AKARI instrument at the given wavelength (Ishihara et al. 2010; Takita et al. 2015). The average sky level was first measured in a circular annulus of inner radius $1.5R_{\text{aper}}$ and outer radius $2.5R_{\text{aper}}$, and was then subtracted from individual measurements. The uncertainty of the total flux density of a given object in a given band was estimated by appropriately propagating the uncertainty on individual measurements, taken as the standard deviation of the flux densities in the same sky annulus. For the FIR 65, 90 and 140 μm bands, the total galaxy flux densities were measured in an identical manner, but without the initial spatial filtering. Details of the measurement will be provided in the AKARI ETG catalogue (Kaneda et al., in preparation), in which integrated flux density measurements of ≈ 8000 ETGs selected from the HyperLeda catalogue (Makarov et al. 2014) will be detailed.

Overall, we measured AKARI flux densities for 258, 260, 245, 246 and 254 of the 260 ATLAS^{3D} ETGs in the 9, 18, 65, 90 and 140 μm bands, respectively, the missing measurements being due to incomplete AKARI sky coverage. When possible, the missing 65 and 90 μm flux densities were replaced by IRAS 60 and/or 100 μm measurements, as listed in the NASA/IPAC Extragalactic Database (NED)¹. In the 65, 90 and 140 μm bands, respectively, a further 52, 8 and 22 measurements are likely affected by source confusion or instrumental artefacts, and are thus excluded from our analysis. The MIR and FIR flux densities thus derived are listed in Table A.1.

¹ <https://ned.ipac.caltech.edu/>

Table 1. AKARI robust detection ($S/N > 3$) statistics.

Band	Detected	Not detected	Not observed	Total
9 μm	106	152	2	260
18 μm	33	227	0	260
65 μm	42	217	1	260
90 μm	111	148	1	260
140 μm	70	184	6	260

Notes. The 14 and 13 galaxies not observed with AKARI in respectively the 65 and 90 μm bands are supplemented by IRAS 60 and/or 100 μm measurements.

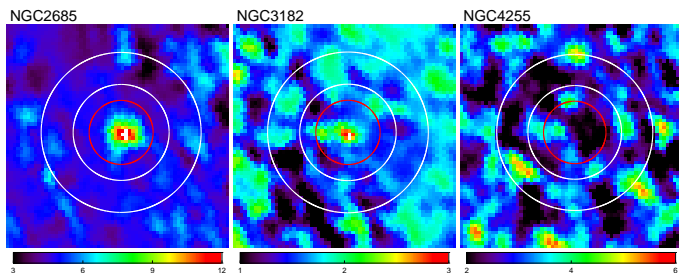


Fig. 1. Examples of galaxies with a strong detection ($S/N > 3$; left), a marginal detection ($S/N \approx 3$; middle) and a non-detection ($S/N < 3$; right) in the 140 μm band. All panels are $16' \times 16'$. Red circles and white annuli show the photometry and sky apertures, respectively. Color bars are in units of MJy sr^{-1} .

It has already been shown that AKARI fluxes are in good agreement with analogous measurements by Spitzer and Herschel (Suzuki et al. 2010; Hattori et al. 2016), but we nevertheless check the quality of our measurement here by comparing our AKARI 90 and 140 μm flux densities with Spitzer and Herschel measurements. Among our sample, 89 galaxies have published Spitzer 70 μm measurements (Amblard et al. 2014), and 22 galaxies have both Herschel 100 and 160 μm measurements (Dale et al. 2012; di Serego Alighieri et al. 2013; Baes et al. 2014). In all cases (AKARI 90 μm vs. Spitzer 70 μm , AKARI 90 μm vs. Herschel 100 μm and AKARI 140 μm vs. Herschel 160 μm), we find that most measurements are consistent within the uncertainties, and that they are proportional with a slope of approximately unity and a small intrinsic scatter of 0.2 dex, thus confirming the reliability of our measurements. These parameters are estimated using a linear fit with free slope and nul intercept in log-log space, adjusting the intrinsic scatter until the reduced χ^2 is equal to 1 (see Williams et al. 2010).

The number of galaxies robustly detected (defined here as having a signal-to-noise ratio $S/N > 3$) is summarised in Table 1 for each band. Detection rates are 41, 13, 16, 43 and 28% for the 9, 18, 65, 90 and 140 μm bands, respectively. In the FIR, 117 galaxies (45%) are detected in at least one band (thus one, two or three FIR bands), while 71 galaxies (27%) are detected in at least two bands (thus two or three FIR bands). The lower detection rates at 18 and 65 μm are due to respectively a relatively high background level (Kondo et al. 2016) and a narrow bandwidth (Kawada et al. 2007). Systematic flux density uncertainties are estimated to be 10% in the MIR (9 and 18 μm ; Ishihara et al., in preparation), and 20, 20 and 50% in the FIR (65, 90 and 140 μm , respectively; Takita et al. 2015). For illustrative purposes, Figure 1 shows an example of a strong detection ($S/N > 3$), a marginal detection ($S/N \approx 3$) and a non-detection ($S/N < 3$), all in the AKARI 140 μm band.

Table 2. Parameters of the best linear fits in Fig. 2.

Band	a	b
9 μm	0.60 ± 0.06	35.24 ± 0.64
18 μm	0.32 ± 0.20	38.18 ± 2.12
90 μm	0.33 ± 0.04	38.24 ± 0.44
140 μm	0.36 ± 0.09	37.77 ± 1.00

Notes. Data points are fit with $\log(L_{\text{IR}}/\text{erg s}^{-1}) = a \log(L_K/L_\odot) + b$.

2.3. WISE survey

Near-infrared (NIR) and MIR flux densities for our sample galaxies are also available from the AllWISE catalog (Cutri et al. 2013), composed of data obtained during the cryogenic and post-cryogenic phases of the WISE all-sky survey. We therefore use the four WISE photometric bands with central wavelengths of 3.4, 4.6, 12 and 22 μm . Total magnitudes were measured using aperture photometry (and are referred to as WXGMAG, with X equal to 1, 2, 3 or 4 for each of the four WISE bands), with the aperture calculated from 2MASS NIR surface photometry (Skrutskie et al. 2006) and the WISE PSF. When a WXGMAG magnitude is not available, we adopt instead the profile fit magnitude WXMPRO. However, as some galaxies are much more spatially extended than the WISE PSF, the profile fit photometry can underestimate the true total fluxes. To avoid this, the WXMPRO magnitudes are calibrated using the method of Griffith et al. (2015), that takes into account the extent of the galaxies as measured from other WISE photometric parameters. Despite this, we use the uncorrected profile fit magnitudes when there is strong contamination from background sources, as the correction process is then likely to be inaccurate. The 2MASS-determined WXGMAG apertures of galaxies that are well resolved spatially can also be slightly too small, resulting in total flux densities underestimated by as much as 30%². We therefore add a systematic uncertainty of 30% to the WISE systematic flux calibration uncertainties.

3. Results

3.1. Relation between IR and K_s -band luminosities

Figure 2 shows correlations between the total 9, 18, 90 and 140 μm AKARI luminosities and the total K_s -band luminosities listed in Cappellari et al. (2011). Luminosities are estimated using the galaxy distances listed in Cappellari et al. (2011) throughout this paper. Data points are colour-coded according to whether the sample galaxies are detected in CO (blue) or not (red) in Young et al. (2011). To quantify the contribution of the stellar emission from old stellar populations to the AKARI luminosities, we fitted the correlations of non-CO-detected galaxies with straight lines. The best fits are shown in the panels of Fig. 2 and the best-fit parameters are listed in Table 2. By subtracting the best fits from the luminosities of CO-detected galaxies, we can estimate their excess luminosities and assess whether these correlate with the K_s -band luminosities. This in turn establishes if the excess luminosities are of (circum)stellar origin or not (and thus of interstellar origin).

As the sample galaxies cover a rather large range of K_s -band luminosities and are spread over that range roughly uniformly in $\log(L_K/L_\odot)$, it is preferable to do the above fits in log-log space (as shown in Fig. 2). While we would ideally use for those fits

² http://wise2.ipac.caltech.edu/docs/release/allsky/expsup/sec6_3e.html

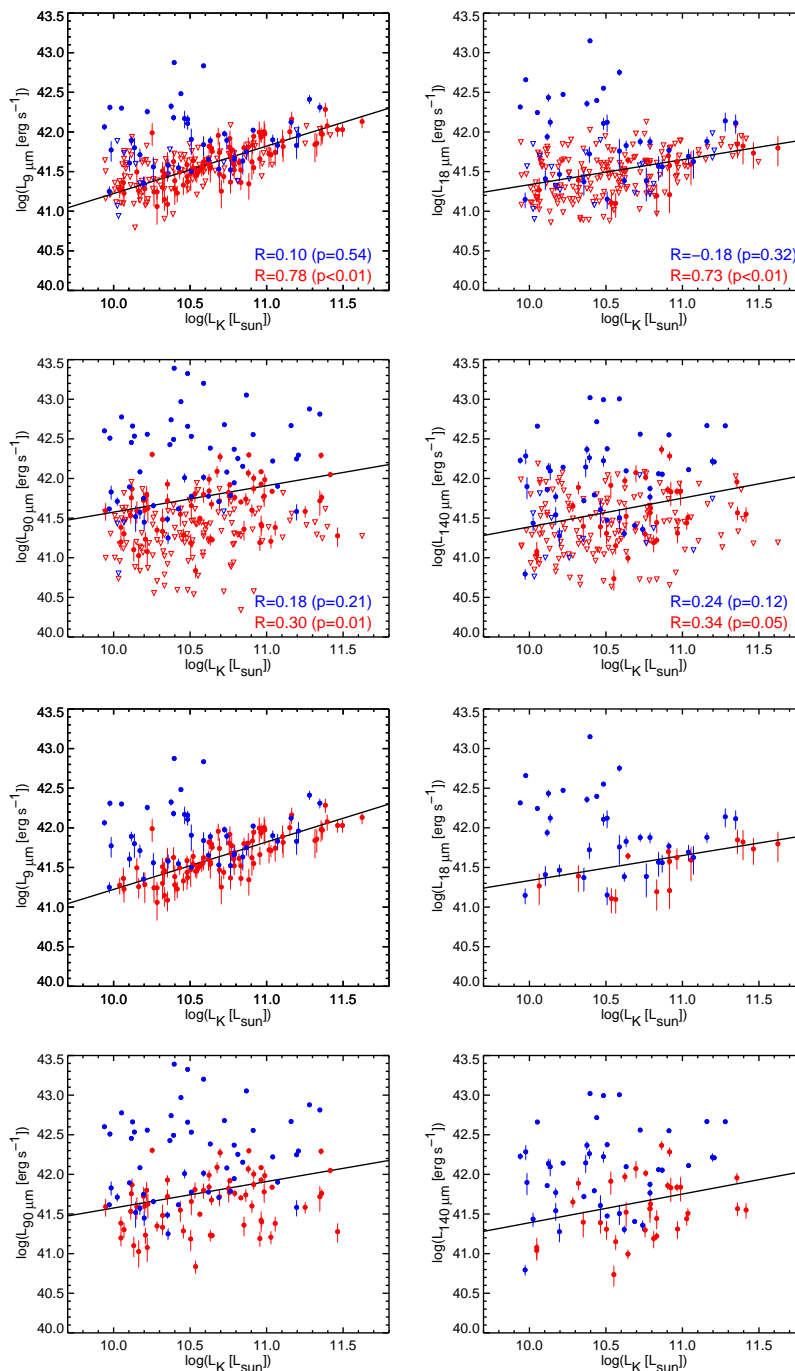


Fig. 2. Total 9, 18, 90 and 140 μm luminosities versus total K_s -band luminosities, for IR measurements with respectively $S/N > 2.4, 2.2, 2.7$ and 2.8 (solid circles). Conversely, open triangles indicate respectively $2.4, 2.2, 2.7$ and 2.8σ upper limits. Blue and red data points denote CO-detected and non-CO-detected galaxies, respectively. Linear correlation coefficients (R) and p -values for CO-detected and non-CO-detected galaxies are indicated in blue and red, respectively, for galaxies above the stated S/N thresholds. Solid black lines show the best linear fits to the non-CO-detected galaxies only, excluding upper limits (see Table 2). The bottom four panels are the same as the top four panels, but without upper limits.

only robustly detected galaxies (i.e., those measurements with $S/N > 3$), this would not leave enough data points for a reliable fit at 18 μm . For each band, we therefore use the lowest S/N threshold yielding only positive measurements ($S/N > 2.4, 2.2, 2.7$ and 2.8 at respectively 9, 18, 90 and 140 μm). The linear correlation coefficients (R) of those measurements and the probabilities of obtaining the measured R if the null hypothesis is true (p) are also listed in each panel, to ascertain the strengths

of the correlations. Measurements below those S/N thresholds are replaced by upper limits of the same significance in Fig. 2.

As can be seen in the top-left panel of Fig. 2, the 9 μm luminosities of non-CO-detected galaxies correlate very well with their K_s -band luminosities (with a correlation coefficient $R = 0.78$ and $> 99\%$ confidence levels). As K_s band traces old stellar populations and the 9 μm emission of non-CO-detected galaxies is also expected to be dominated by emission from the stars themselves, a correlation between these two bands is

expected. However, CO-detected galaxies show excess 9 μm emission, being systematically above the correlation of non-CO-detected galaxies (or consistent with it), suggesting that CO-detected galaxies have PAH emission beyond any associated with the stars. Indeed, the AKARI 9 μm band is sensitive to major PAH bands at 6.2, 7.7 and 8.6 μm (Ishihara et al. 2010). Furthermore, the excess luminosities of CO-detected galaxies do not correlate well with their K_s -band luminosities ($R = -0.14$ and $p = 0.36$), suggesting that their PAHs are not of circumstellar origin but rather of interstellar origin.

The correlation between the 18 μm and K_s -band luminosities is also significant for non-CO-detected galaxies ($R = 0.73$ and $p < 0.01$; top-right panel of Fig. 2), suggesting that the bulk of their 18 μm emission is of circumstellar dust origin. This is supported by the fact that circumstellar dust generated and heated by old stars is known to be the dominant emission source in ETGs at 15 and 24 μm (Athey et al. 2002; Temi et al. 2009). Most CO-detected galaxies again show a significant excess above the correlation of non-CO-detected galaxies, and their excess luminosities is not correlated with their K_s -band luminosities ($R = -0.18$ and $p = 0.32$). The 18 μm emission of CO-detected galaxies is thus likely due to interstellar dust heated by relatively young stellar populations or AGN activity (see Nyland et al. 2016 for a study of nuclear radio emission in ATLAS^{3D} ETGs). The 9 and 18 μm luminosities thus strongly suggest that ETGs with detectable molecular gas also contain significant interstellar dust.

In the bottom two panels of Fig. 2, the correlations between the FIR 90 and 140 μm luminosities (tracing cold dust) and the NIR K_s -band luminosities (tracing stellar emission) of non-CO-detected galaxies are weaker than those in the MIR bands and are not statistically significant. This appears consistent with the results of Temi et al. (2007), who argued that FIR emission in ETGs originates from cold dust of interstellar origin, presumably spread and heated by diffuse starlight and/or hot gas. However, it is worth noting that the correlations are not totally negligible either ($p = 0.01$ and 0.05 at 90 and 140 μm , respectively). This raises the interesting possibility that the stellar populations of ETGs may have cold dust of circumstellar origin, perhaps in shells at large stellar-centric radii. This should however be verified with either more accurate or more numerous data. Either way, CO-detected galaxies again show systematically brighter FIR emission, uncorrelated with stellar emission, implying that they are even richer in interstellar cold dust than the norm (i.e., than non-CO-detected galaxies).

3.2. PAH and dust emission

To estimate accurate PAH and dust luminosities for our sample galaxies, we created spectral energy distributions (SEDs) by combining the 2MASS K_s -band, WISE and AKARI data. We fitted each SED with a model composed of emission from stars, PAHs and two dust components (warm and cold). We described the stellar continuum emission with a power-law model. In addition, to describe a silicate feature seen in ETGs around 10 μm (e.g., Bressan et al. 2006), we added a Gaussian function to the power-law model, where the width and amplitude of the Gaussian relative to the stellar continuum were determined from the quiescent elliptical galaxy template of Kaneda et al. (2008). The Draine & Li (2007) model was used for the PAH emission, with a size distribution and ionised fraction typical of the diffuse ISM of star-forming galaxies (for lack of a better model), while only the amplitude was allowed to vary. The warm and cold dust components were each described by a modified blackbody model with emissivity power-law index 2 (Galametz et al. 2012), while

the amplitude and temperature were allowed to vary. When fitting the SEDs, we used all detections regardless of their significance, adopting their errors as weights ($1/\sigma^2$, where σ is the error), with the additional constraint that the fits must be positive at all wavelengths.

First, we fitted the SEDs of galaxies robustly detected (i.e., $S/N > 3$) in two or three FIR bands, by allowing all the parameters to vary. Then, by fixing the warm and cold dust temperatures to the means of the best-fit temperatures of those galaxies, we fitted the SEDs of the remaining galaxies (i.e., galaxies detected in only one or no FIR band). Although this ignores the differences between random and systematic uncertainties and is therefore not ideal, we added the measurement and systematic flux calibration uncertainties in quadrature when performing the fits.

In our sample, 71 galaxies are robustly detected in two or three FIR bands, from which we estimated a mean dust temperature of 83 ± 22 K for the warm component and 26 ± 6 K for the cold component. The fit was not acceptable at the 90% confidence level for 3 of these objects. For the remaining galaxies, the fit was not acceptable for 26 objects. These 29 objects were thus excluded from the following analysis. The SEDs and best-fit models of the 231 remaining ATLAS^{3D} ETGs are shown in Fig. 3.

We calculated the PAH and dust luminosities (L_{PAH} , L_{warm} and L_{cold}) by integrating the aforementioned best-fits of each component over the wavelength range 5–1000 μm . The luminosities thus derived are listed in Table A.2, and the total IR (TIR) luminosities (L_{TIR}) were estimated by simply taking the sums of those three components. To check the reliability of our PAH luminosities, we compared them to the PAH luminosities derived by Shapiro et al. (2010) using the non-stellar Spitzer 8 μm emission (as done in Sect. 2.2 for our 90 and 140 μm flux densities). The PAH luminosities are almost all consistent within the uncertainties, and are proportional with a slope of approximately unity and a small intrinsic scatter of 0.2 dex. Figure 4 shows L_{PAH} , L_{warm} , L_{cold} and L_{TIR} plotted against H_2 mass, the latter calculated from the integrated CO line intensity assuming a Galactic conversion factor (see Young et al. 2011). It is clear that the IR luminosities of CO-detected galaxies (here stellar emission-subtracted by construction) are well correlated with their molecular gas masses, thus confirming a tight connection between dust and molecular gas even in ETGs (see also Combes et al. 2007). Among the IR luminosities, L_{warm} has a relatively large scatter, suggesting that dust heating by young stellar populations and/or AGN can vary from galaxy to galaxy.

3.3. Star formation rates

To estimate the current SFRs of the 231 ATLAS^{3D} ETGs with good SED fits, we utilised the PAH and TIR luminosities calculated from those fits. In particular, ionised PAHs are known to be good tracers of star formation, as they are exposed to the radiation fields of photo-dissociation regions around relatively young stars, and the AKARI 9 μm band is sensitive to the 6.2, 7.7 and 8.6 μm features of ionised PAHs (Ishihara et al. 2010). We note that relatively quiescent ETGs tend to show unusually high PAH 11.3 μm /PAH 7.7 μm ratios, indicating a dominance of neutral PAHs not related to star formation (e.g., Kaneda et al. 2005, 2008; Panuzzo et al. 2011), but our results are not likely to be sensitive to this unusual interband ratio as L_{PAH} is mostly determined from the AKARI 9 μm band that excludes the 11.3 μm feature. Furthermore, the WISE 12 μm -band fluxes do not indicate the presence of unusually strong PAH 11.3 μm features.

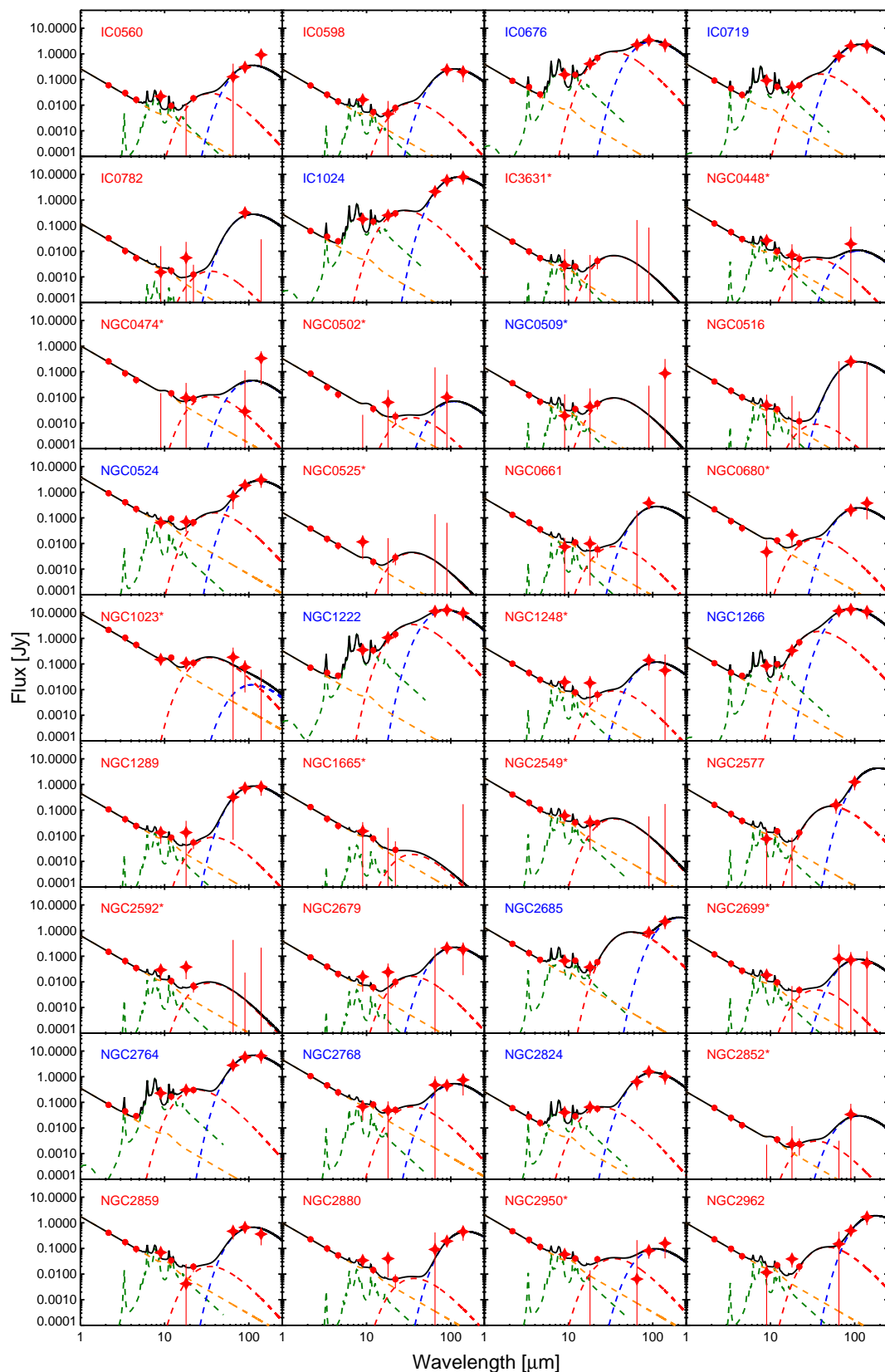


Fig. 3. Observed spectral energy distributions (red data points) overlaid with the best-fit spectral models (solid black lines), for the 231 successfully fitted ATLAS^{3D} galaxies. AKARI data points are shown as stars, others data points as filled circles. Dotted orange, green, red and blue lines indicate the best-fit stellar, PAH, warm and cold dust component, respectively. The name of the galaxy is indicated in the top-left corner of each panel, in blue for CO-detected galaxies and red for non-CO-detected galaxies. Galaxies with no AKARI FIR (65, 90 or 140 μm) detection are marked with an asterisk.

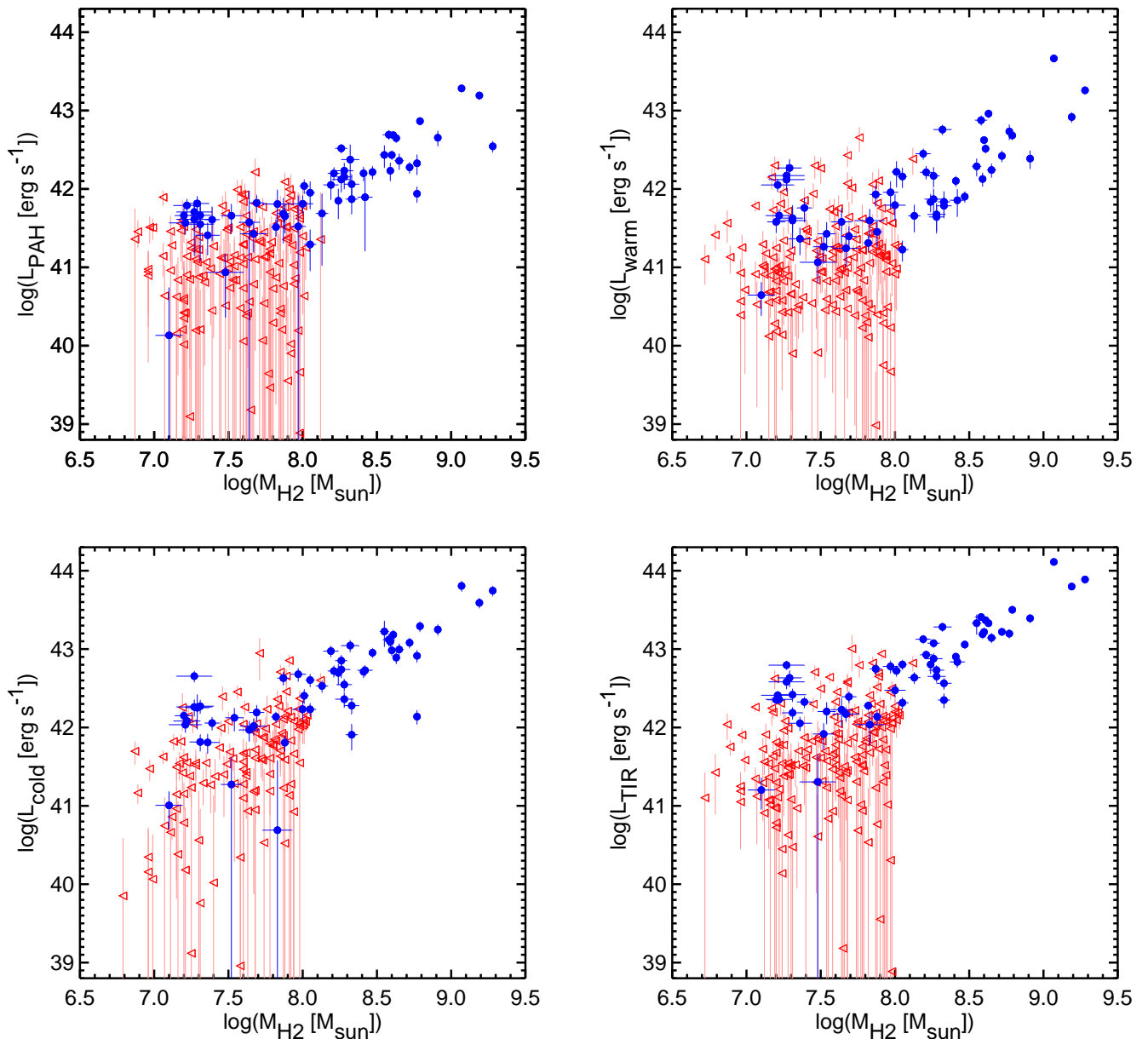


Fig. 4. Infrared-derived luminosities (PAH, warm dust, cold dust and TIR) versus molecular gas (H_2) masses, for the 231 successfully fitted ATLAS^{3D} galaxies. Blue data points represent CO-detected galaxies while open red triangles show non-CO-detected galaxies (i.e., M_{H_2} upper limits).

To convert L_{PAH} to a SFR, we adopted the method described in Shipley et al. (2016), in which the sum of the 6.2, 7.7 and 11.3 μm features is used to estimate the SFR. The ratio of these PAH bands to the total PAH emission is 0.65 in the PAH template adopted for our SED fits (a value typical of star-forming galaxies; Smith et al. 2007), so we simply propagate this fraction in our calculations. To convert L_{TIR} to a SFR, we used the conversion of Kennicutt (1998) with a correction to the Kroupa initial mass function (Hao et al. 2011; Murphy et al. 2011).

For the majority of our 231 ETGs, the current SFR is estimated to be in the range $0.01 - 1 M_{\odot} \text{yr}^{-1}$. Furthermore, as shown in the right panel of Fig. 5, the SFRs estimated from PAH luminosities are in good agreement with those estimated from TIR luminosities, with an average ratio of $\text{SFR}_{PAH}/\text{SFR}_{TIR} = 1.0 \pm 0.1$

and nul intrinsic scatter (given the large uncertainties; estimated again as in Sect. 2.2).

For 56 CO-detected ETGs of the ATLAS^{3D} sample, Davis et al. (2014) estimated the current SFR with a combination of FUV and 22 μm emission. In the left and middle panels of Fig. 5, we therefore compare those SFRs with the PAH and TIR SFRs calculated here. Our SFRs are generally in good agreements with those of Davis et al. (2014), but they are systematically larger by a factor of ≈ 2 at SFRs smaller than $\approx 0.1 M_{\odot} \text{yr}^{-1}$ ($\text{SFR}_{PAH}/\text{SFR}_{FUV+22\mu\text{m}} = 1.6 \pm 0.2$ and $\text{SFR}_{TIR}/\text{SFR}_{FUV+22\mu\text{m}} = 2.2 \pm 0.3$, with intrinsic scatters of 0.3 dex, for all galaxies in common). This systematic difference is presumably due to the specific physical conditions in the star-formation regions of ETGs, that will be discussed in Sect. 4.3.

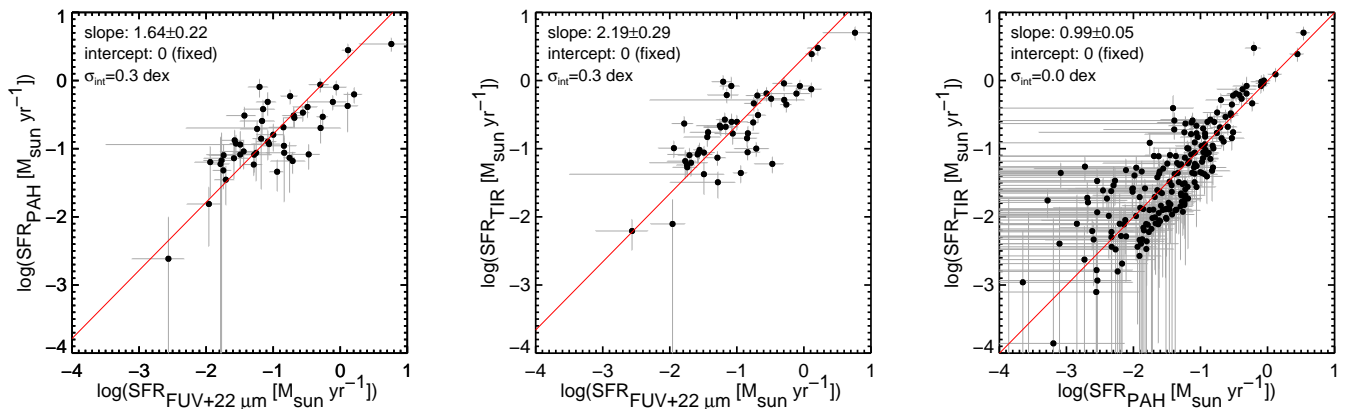


Fig. 5. Comparisons of our PAH- and TIR-derived star formation rates and the FUV+22 μm star formation rates of Davis et al. (2014), the latter for CO-detected galaxies only. Solid red lines show the best-fit linear relations with nul intercepts, while the labels list the best-fit slopes, fixed intercepts and intrinsic scatters around the best-fit relations.

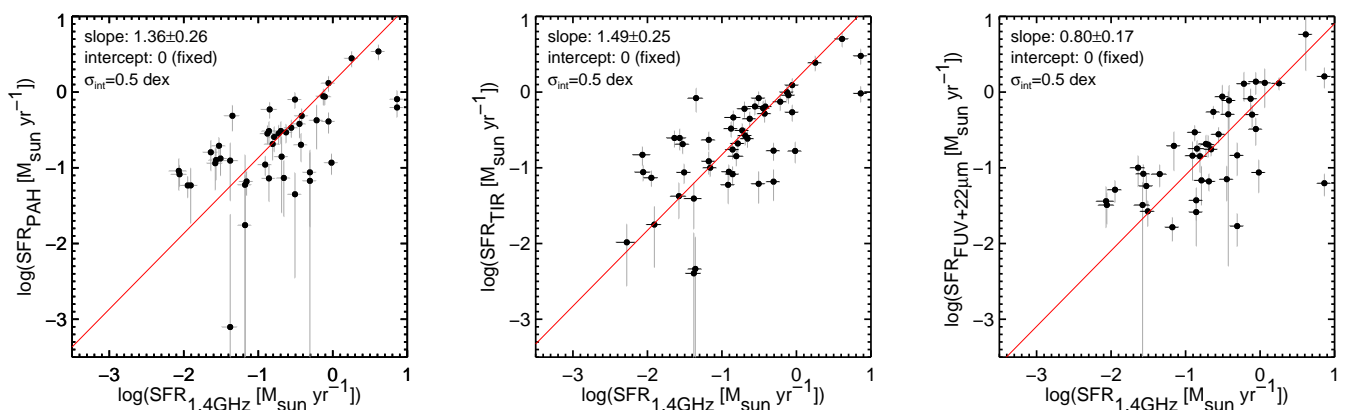


Fig. 6. Comparisons of our PAH- and TIR-derived star formation rates and the FUV+22 μm star formation rates of Davis et al. (2014) with 1.4 GHz star formation rates derived from the measurements of Nyland et al. (2017), for all galaxies in common. Solid red lines show the best-fit linear relations with nul intercepts, while the labels list the best-fit slopes, fixed intercepts and intrinsic scatters around the best-fit relations.

Low-frequency (1.4 GHz) radio continuum observations of 72 ATLAS^{3D} ETGs were presented by Nyland et al. (2017). We therefore estimated SFRs from these measurements using the conversion of Murphy et al. (2011), and we compare these estimates with our PAH- and TIR-derived estimates in Fig. 6. As shown in the left and middle panels, our measurements are generally in good agreements with those derived from Nyland et al. (2017), but they are systematically larger by factors of $\text{SFR}_{\text{PAH}}/\text{SFR}_{1.4\text{GHz}} = 1.4 \pm 0.3$ and $\text{SFR}_{\text{TIR}}/\text{SFR}_{1.4\text{GHz}} = 1.5 \pm 0.3$, with intrinsic scatters of 0.5 dex (for all galaxies in common). As can be expected from the discussion in the paragraph above, the 1.4 GHz- and FUV+22 μm -derived SFRs are then in rough agreement ($\text{SFR}_{\text{FUV}+22\mu\text{m}}/\text{SFR}_{1.4\text{GHz}} = 0.8 \pm 0.2$, with an intrinsic scatter of 0.5 dex for galaxies in common; see the right panel of Fig. 6). These results will also be discussed in Sect. 4.3.

4. Discussion

4.1. Relations between SFRs and gas masses

Star formation in galaxies is characterized by a power-law relation between the current SFR (Σ_{SFR}) and cold gas mass (Σ_{gas}) surface densities, known as the Kennicutt-Schmidt (KS) law ($\Sigma_{\text{SFR}} \propto \Sigma_{\text{gas}}^n$), where the power-law index n is found to be

≈ 1.4 for local star-forming galaxies (Kennicutt 1998) but varies from 1 to 2 from galaxy to galaxy, reflecting differences in the star formation processes (e.g., Taniguchi & Ohyama 1998; Misiriotis et al. 2006). The power-law index is also generally closer to unity for molecules tracing gas denser than CO (e.g., HCN; Gao & Solomon 2004). Davis et al. (2014) investigated the KS law of 56 CO-detected ATLAS^{3D} galaxies using their SFRs estimated from FUV and 22 μm emission. Here, we revisit the KS law for the same 56 ETGs using our SFRs estimated from PAH and TIR emission.

To calculate Σ_{SFR} and Σ_{gas} , we use our own SFRs but the gas masses and source sizes listed in Davis et al. (2014), where the gas masses were derived by summing the CO and central H I gas masses, and the sizes were measured using interferometric CO, spatially-resolved MIR, optical or FUV observations. The resulting $\Sigma_{\text{SFR}} - \Sigma_{\text{gas}}$ correlations are shown in Fig. 7. The solid black lines and shaded grey regions show respectively the KS law of local star-forming galaxies with $n = 1.4$ and its intrinsic scatter (Kennicutt 1998). The solid and dashed red lines show the best linear fits to the data with respectively free and fixed ($n = 1.4$) slope. The best-fit parameters are listed in Table 3. We note that the galaxy NGC 1266, that is systematically located in the top-right of each panel of Fig. 7, is known to have strongly suppressed star formation and thus to be an out-

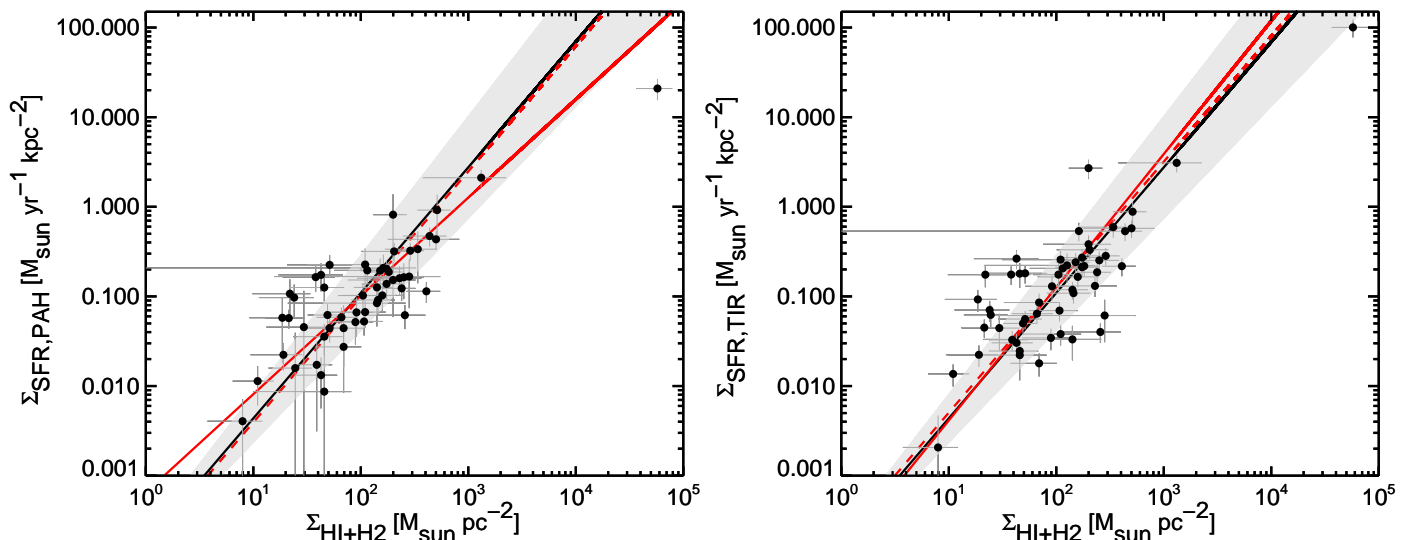


Fig. 7. Star formation rates (PAH- and TIR-derived) versus total gas surface densities (i.e., KS law) for CO-detected galaxies. Solid black lines and shaded grey regions show respectively the Kennicutt (1998) relation for local star-forming galaxies (with power-law index $n = 1.4$) and its intrinsic scatter. Solid and dashed red lines show the best linear fits with respectively free and fixed ($n = 1.4$) slope. The galaxy located in the top-right of each panel is NGC 1266, known to have strongly suppressed star formation. It was excluded from the fits.

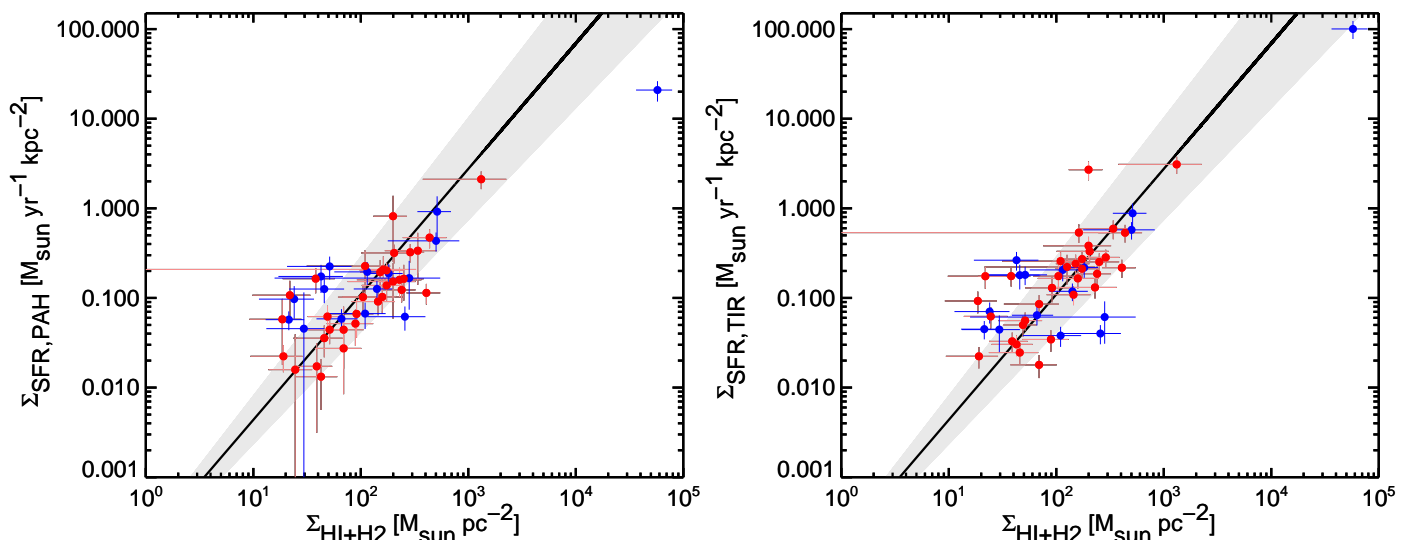


Fig. 8. Same as Fig. 7, but with galaxies with kinematically-aligned and misaligned stars and ionised gas shown in red and blue, respectively.

lier in the star-formation relation (see Alatalo et al. 2011, 2015; Nyland et al. 2013). We have thus excluded it from the fits. Figure 7 shows that the majority of CO-detected (and thus potentially star-forming) ETGs do follow the KS law of local star-forming galaxies. In particular, the fixed-slope fits have no offset with respect to the Kennicutt (1998) relation, suggesting that the SFEs of local ETGs are similar to those of local star-forming galaxies. This is contrary to the results of Davis et al. (2014), that suggested smaller SFEs for the same sample galaxies, by a factor of 2–3. This difference can be directly attributed to the similarly higher SFRs calculated here from the AKARI data (see Sect. 3.3 and Figs. 5 and 6). We come back to this difference in Sect. 4.3.

When left free, the slopes of the power-law fits are $n = 1.10 \pm 0.11$ and $n = 1.49 \pm 0.13$ for the PAH and TIR SFRs,

Table 3. Parameters of the best linear fits in Fig. 7.

SFR tracer	n	c
PAH	1.10 ± 0.11	-3.19 ± 0.26
PAH	1.40 (fixed)	-3.81 ± 0.04
Total IR	1.49 ± 0.13	-3.87 ± 0.27
Total IR	1.40 (fixed)	-3.70 ± 0.03

Notes. Data points are fit with $\log(\Sigma_{\text{SFR}}/M_{\odot} \text{pc}^{-2}) = n \log(\Sigma_{\text{gas}}/M_{\odot} \text{pc}^{-2}) + c$.

respectively. The significant deviation of the PAH SFR slope from $n = 1.4$ appears to be caused by several galaxies with relatively high Σ_{SFR} at $\Sigma_{\text{gas}} \lesssim 0.6 \times 10^2 M_{\odot} \text{pc}^{-2}$. Those galaxies may have a different star-formation mode (e.g., widespread

versus circumnuclear) or a different ISM-acquisition mode (e.g., internal versus external). The origin of the gas can be constrained by examining the kinematic misalignment between stars and gas. Kinematically-misaligned gas likely indicates an external origin (e.g., minor merger or accretion from filaments), while kinematically-aligned gas is expected from both internal (e.g., stellar mass loss or remnant from the galaxy formation event) and occasionally external gas. Figure 8 is analogous to Fig. 7, but we colour code the galaxies according to their star-ionised gas kinematic (mis)alignment, when such a measurement is available. Davis et al. (2011) measured star-gas kinematic (mis)alignments for 35 CO-detected galaxies mapped interferometrically in CO, but 51 CO-detected galaxies mapped with optical integral-field spectroscopy in ionised gas, and they showed that both measurements are always in agreement. We therefore use the latter measurements here. Interestingly, Fig. 8 reveals that many of the galaxies with relatively high Σ_{SFR} at $\Sigma_{\text{gas}} \lesssim 0.6 \times 10^2 M_{\odot} \text{pc}^{-2}$ (and none of the galaxies with relatively low Σ_{SFR} at those same Σ_{gas}) have kinematically-misaligned gas, indicating that they have acquired their ISM from external sources. Galaxies with kinematically-misaligned gas also seem to have higher scatters around the best-fit relations than galaxies with kinematically-aligned gas, perhaps suggesting a more bursty and thus temporally variable recent star formation history.

4.2. Relations between SFRs and stellar masses

In Fig. 9, the PAH and TIR SFRs of our sample galaxies are plotted against their stellar masses M_{\star} , the latter calculated from optical photometry and stellar mass-to-light ratios measured from dynamical models (Cappellari et al. 2013). The data points are also colour-coded according to the mass-weighted stellar population age of each galaxy, obtained by fitting stellar population synthesis models to the optical spectrum of the inner effective radius (McDermid et al. 2015). We use mass-weighted ages rather than the more common luminosity-weighted ages as the former better represent the age of the bulk of the stellar populations, being less affected by a sprinkling of young stars onto a dominant old stellar population. The dotted black lines show the so-called star-formation main sequence, i.e., the correlation between current SFR and stellar mass of local star-forming galaxies (Elbaz et al. 2007). The dotted blue, green and red lines are linear fits to our ETG galaxies in the age range 3–7, 7–11 and 11–14 Gyr, respectively. The best-fit parameters are listed in Table 4. A similar figure for the SAURON sample of 48 ETGs was presented by Shapiro et al. (2010), but the much larger ATLAS^{3D} sample of 260 ETGs studied here (231 with relevant measurements) offers much clearer insight into the relationship between current SFR, stellar mass and stellar population age.

Figure 9 shows that, at fixed stellar mass, all our sample ETGs have a lower current SFR than that of local star-forming galaxies, confirming that local ETGs are quiescent galaxies. Figure 9 also shows that, overall (and at least in the recent history of the universe), the SFRs of ETGs must decrease as they evolve (i.e., ETGs move to the lower-right of the panels as they become older and more massive). However, while at fixed mass the current SFRs decrease strongly with age (here by about 1.5 dex), at fixed stellar age the current SFRs increase with stellar mass. In fact, at fixed stellar age the SFRs and stellar masses of our ETGs are correlated similarly to those of local star-forming galaxies, with power-law slopes near unity (see Table 4). This is shown more clearly in Fig. 10, that shows the specific SFRs (sSFRs, i.e., SFR/M_{\star}) of our sample galaxies as a function of stellar mass. Indeed, while the current sSFRs of our ETGs strongly decrease

with age as expected from Fig. 9, they are nearly independent of stellar mass at any age. Similar trends are reported for galaxies with low SFRs by Saintonge et al. (2016), who studied both early- and late-type galaxies (see their Figs. 2 and 4). This suggests that local ETGs acquire their cold ISM necessary to form stars by mechanisms related to stellar mass, as do normal star-forming galaxies (e.g., Davé et al. 2011).

We note here that the sSFRs and stellar ages we discuss are independent of each other and are not correlated by construction. As our SFRs (estimated from MIR photometry) trace only young stars while our total stellar masses (estimated from optical photometry and stellar dynamical modelling) include both young and old stars, our sSFRs trace the ratio of young to both young and old stars. On the other hand, our stellar ages (estimated from optical spectroscopy) trace the ratio of young to old stars only. Our SFRs are also (nearly) instantaneous measures (tracing stars of ages typically < 100 Myrs), while our stellar ages are also affected by (and nearly always degenerate with) intermediate age stars (≥ 1 Gyr).

4.3. Star formation in ETGs

Based on current SFRs estimated from FUV and 22 μm emission, Davis et al. (2014) argued that local ETGs have SFEs lower than those of local star-forming galaxies, an effect they assigned to the particular dynamical properties of ETGs, such as increased central disc stability and/or galactic shear in the central regions where molecular gas is found. However, our results show that the SFEs of (the same) local ETGs estimated from AKARI PAH and TIR emission are similar to those of local star-forming galaxies (see Figs. 5 and 7), in agreement with the smaller study of Shapiro et al. (2010) utilizing Spitzer PAH emission. As TIR emission can be enhanced by low-luminosity AGN and old stellar populations, that are unrelated to star-formation, the discrepancy of the TIR-estimated SFRs is likely easily explained. The discrepancy of the PAH-estimated SFRs is however not so easily explained, and may be due to the fact that PAH emission (like TIR emission) can trace star-formation regions with softer UV radiation fields than those traced in the FUV and at 22 μm (e.g., Compiègne et al. 2011). The higher PAH SFRs therefore apparently call for less massive star formation. Indeed, it is suggested that galaxies with low SFRs preferentially form low-mass stars (rather than high-mass stars; e.g., Hoversten & Glazebrook 2008; Gunawardhana et al. 2011), which would result in softer radiation fields in ETGs. The ratios of the [C II] 158 μm line to FIR fluxes also support radiation fields softer in ETGs than in spiral galaxies (Malhotra et al. 2000). While old stars in ETGs can and do emit in the UV (UV-upturn phenomenon; Yi et al. 1997), Davis et al. (2014) argued that this does not significantly affect the FUV-based SFRs of the ATLAS^{3D} ETGs. Interestingly, this preference for low-mass stars is consistent with a flurry of recent works arguing that ETGs have bottom-heavy initial mass functions (IMFs; see, e.g., van Dokkum & Conroy 2010; Cappellari et al. 2012).

Of course, just like the FUV and 22 μm estimates, the 1.4 GHz SFR estimates derived from the Nyland et al.'s (2017) radio continuum measurements are also systematically lower than the PAH- and TIR-derived estimates (see Fig. 6). As the 1.4 GHz continuum emission is due to non-thermal synchrotron emission associated with supernova remnants (and thus ultimately the explosions of massive stars; e.g., Murphy et al. 2011), this trend is also consistent with a scenario whereby massive star formation is inefficient in ETGs.

Table 4. Parameters of the best linear fits in Fig. 9.

SFR tracer	Mass-weighted age (Gyr)	a	b
PAH	3–7	0.93 ± 0.23	-10.12 ± 2.33
PAH	7–11	0.72 ± 0.20	-8.32 ± 2.10
PAH	11–14	1.09 ± 0.22	-12.94 ± 2.43
Total IR	3–7	0.80 ± 0.17	-8.82 ± 1.71
Total IR	7–11	0.76 ± 0.13	-8.95 ± 1.37
Total IR	11–14	0.84 ± 0.09	-10.32 ± 1.04

Notes. Data points are fit with $\log(\text{SFR}/M_\odot \text{ yr}^{-1}) = a \log(M_\star/M_\odot) + b$.

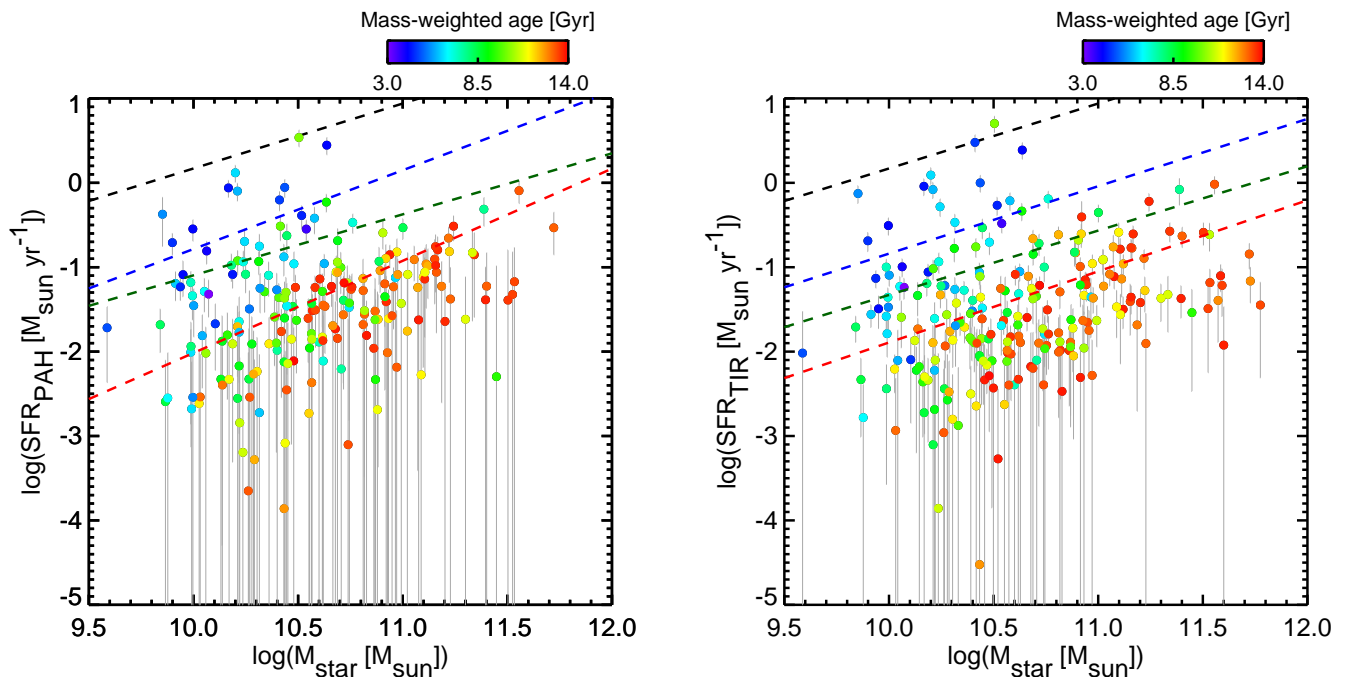


Fig. 9. Correlations between the star formation rates (PAH- and TIR-derived) and stellar masses of the 231 successfully fitted ATLAS^{3D} galaxies. Data points are colour-coded according to their mass-weighted stellar population age (McDermid et al. 2015). Dotted black lines show the star formation main sequence of local star-forming galaxies (Elbaz et al. 2007). Dotted blue, green and red lines show the best linear fits for the age range 3–7, 7–11 and 11–14 Gyr, respectively.

Figure 11 shows the current SFEs of CO-detected ETGs as a function of their stellar masses, with the data points colour-coded as a function of mass-weighted stellar age. No dependence is apparent as a function of either stellar mass or age. Combined with the continuous decrease of the $s\text{SFR} - M_{\text{star}}$ relations with stellar age seen in Fig. 10, this implies that the current cold gas fraction (M_{gas}/M_\star) of ETGs must decrease with stellar age (at fixed stellar mass; $s\text{SFR} \equiv \text{SFR}/M_\star = \text{SFE} \times M_{\text{gas}}/M_\star$). We show this trend in Fig. 12, where M_{gas}/M_\star is plotted as a function of mass-weighted stellar age. The same trend is reported for nearby massive galaxies ($\log(M_\star/M_\odot) > 10$) by Saintonge et al. (2011, 2016), although our study extends the trend to lower gas fractions ($M_{\text{gas}}/M_\star \approx 10^{-4}$). Hence our results suggest that the decrease of the current SFR in local ETGs is likely due to a decrease of their cold gas fractions, rather than a suppression of star formation (via, e.g., AGN feedback or specific dynamical properties).

5. Conclusions

We have conducted a systematic study of star formation in the 260 local ETGs of the ATLAS^{3D} survey, using newly measured IR fluxes from the AKARI all-sky diffuse maps combined with WISE and 2MASS literature data. In the AKARI FIR bands, 117 (45%) galaxies are detected in at least one band, while 71 (27%) galaxies are detected in at least two bands. The 9 and 18 μm luminosities of the non-CO-detected galaxies are correlated with the stellar luminosities, showing that they trace respectively stellar and circumstellar dust emission. On the other hand, CO-detected galaxies show an excess above these correlations, uncorrelated with the stellar luminosities, indicating that they likely contain PAHs and dust of interstellar origin. There are at best weak correlations between the 90 and 140 μm luminosities and the stellar luminosities of non-CO-detected galaxies (but again an excess for CO-detected galaxies), suggesting that FIR emission in ETGs primarily originates from cold dust unrelated to the stars.

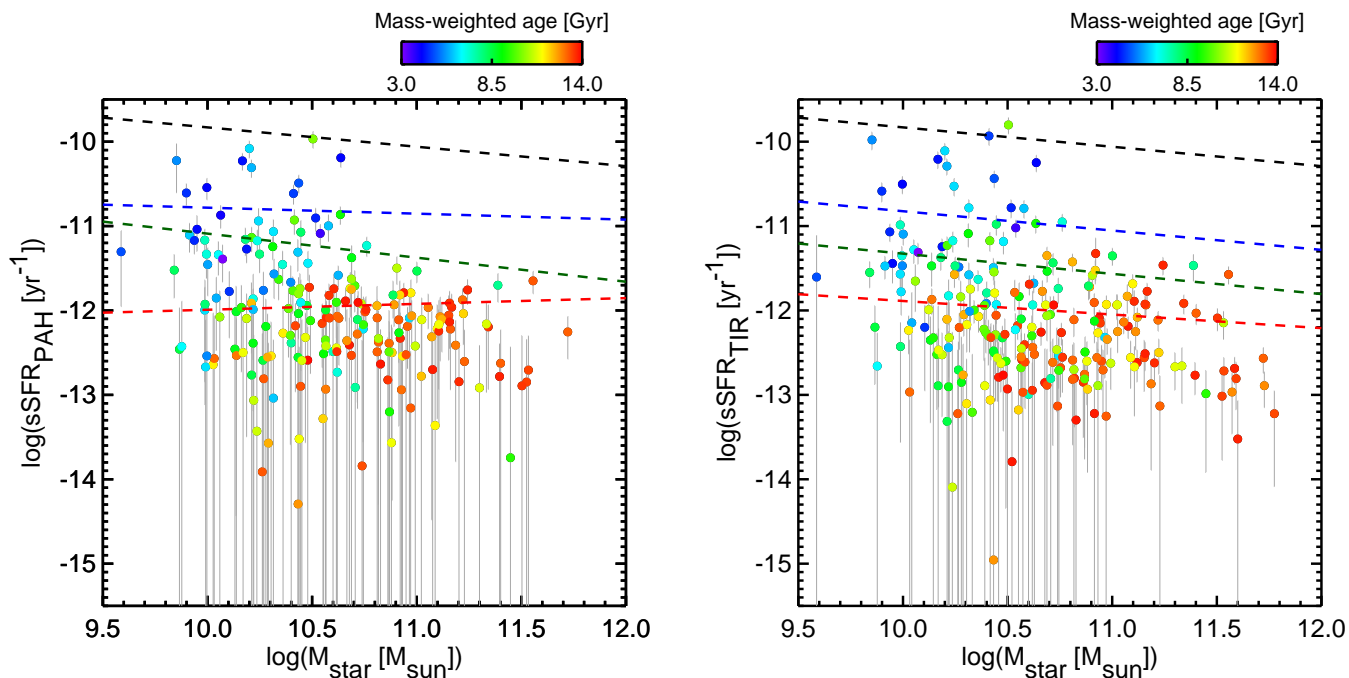


Fig. 10. Same as Fig. 9, but for the specific star formation rates.

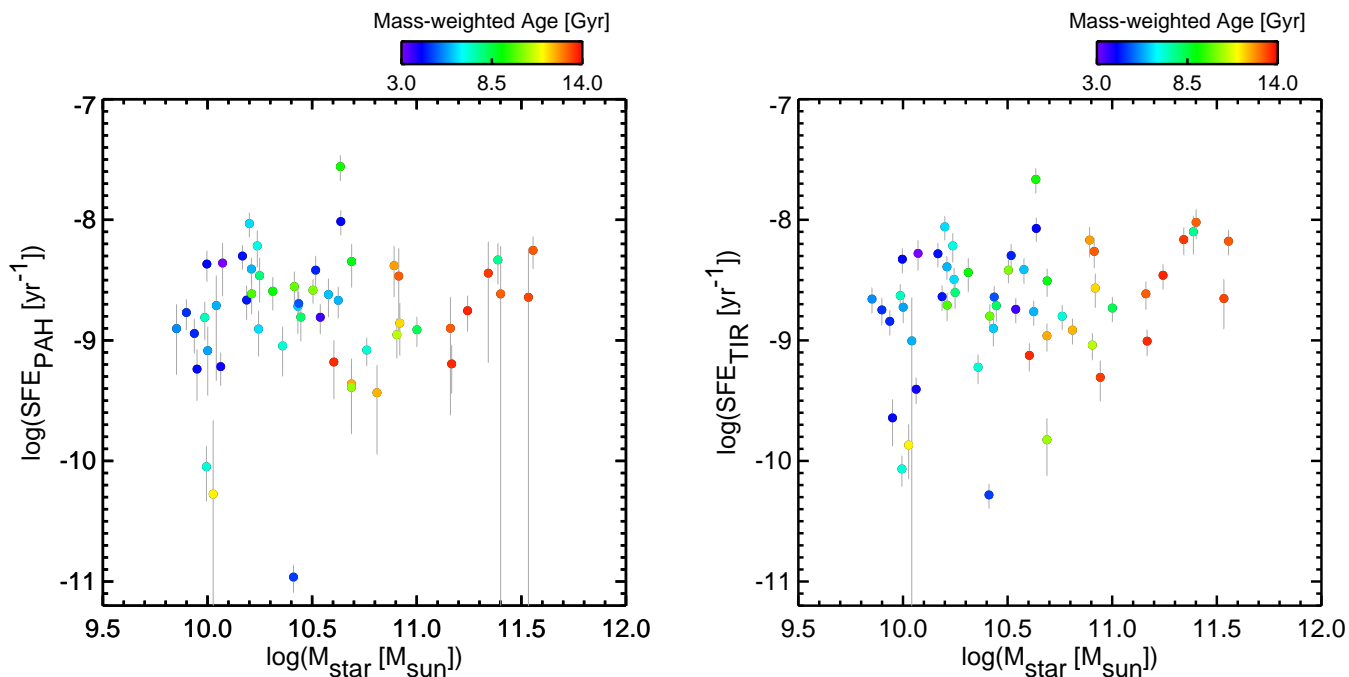


Fig. 11. Star formation efficiencies (PAH- and TIR-derived) versus stellar masses for CO-detected galaxies. Data points are colour-coded according to their mass-weighted stellar population age (McDermid et al. 2015), as in Fig. 9.

We estimated the IR luminosities (L_{PAH} , L_{warm} , L_{cold} and L_{TIR}) of the sample ETGs by decomposing their SEDs with a dust model. For the CO-detected galaxies, all of the IR luminosities correlate well with the H_2 masses, confirming a tight connection between interstellar dust and molecular gas in local ETGs.

Utilizing L_{PAH} and L_{TIR} as current SFR indicators, we measure typical current SFRs of $0.01 - 1 M_{\odot} \text{ yr}^{-1}$. These SFRs are generally in good agreement with previously measured SFRs using FUV and $22 \mu\text{m}$ emission as well as 1.4 GHz radio continuum emission, but they are systematically higher by a factor of $\approx 1.5 -$

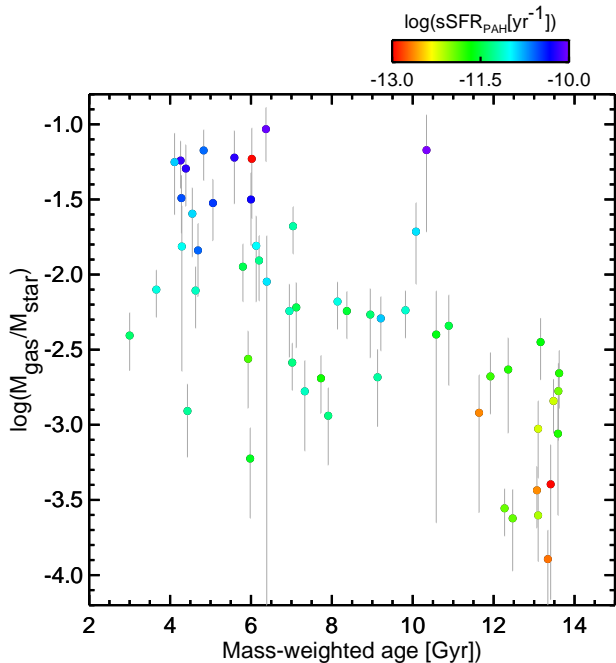


Fig. 12. Cold gas fraction versus mass-weighted stellar population age (McDermid et al. 2015) for CO-detected galaxies. Data points are colour-coded according to their PAH-derived specific star formation rates.

2, particularly at low SFRs. This discrepancy may be due to the fact that PAH and TIR emission can trace star-formation regions with softer radiation fields than those traced in the FUV, $22\ \mu\text{m}$ and 1.4 GHz bands. The majority of ETGs appear to follow the standard KS law of local star-forming galaxies, with no offset, indicating that they have similar current SFEs. This is contrary to recent results suggesting slightly lower SFEs, and is directly related to the higher SFRs derived. There is also some evidence that ETGs whose cold gas has an external origin have more varied SFEs.

We have also investigated the relations between current SFRs, stellar masses and mass-weighted stellar population ages. At fixed stellar mass, the SFRs rapidly decrease with age, but at fixed stellar age the SFRs are roughly linearly correlated with stellar mass, indicating roughly constant sSFRs. In addition, the current SFEs of CO-detected galaxies appear independent of both stellar age and mass. These results suggest that local ETGs acquire their cold ISM by mechanisms regulated primarily by stellar mass, while at fixed stellar mass the cold gas fraction must decrease with stellar age. Hence the current relatively low SFRs of local ETGs are likely due to a decrease of their cold gas fractions, rather than a suppression of star formation.

Acknowledgements. This research is based on observations with AKARI, a JAXA project with the participation of ESA, and has made use of the NASA/IPAC Infrared Science Archive and Extragalactic Database (NED), both of which are operated by the Jet Propulsion Laboratory, California Institute of Technology, under contract with the National Aeronautics and Space Administration. T.K. is financially supported by Grants-in-Aid for JSPS Fellows No. 26003136.

References

- Alatalo, K., Blitz, L., Young, L. M., et al. 2011, *ApJ*, 735, 88
 Alatalo, K., Davis, T. A., Bureau, M., et al. 2013, *MNRAS*, 432, 1796
 Alatalo, K., Lacy, M., Lanz, L., et al. 2015, *ApJ*, 798, 31
 Amblard, A., Riguccini, L., Temi, P., et al. 2014, *ApJ*, 783, 135
 Athey, A., Bregman, J., Bregman, J., Temi, P., & Sauvage, M. 2002, *ApJ*, 571, 272
 Bacon, R., Copin, Y., Monnet, G., et al. 2001, *MNRAS*, 326, 23
 Baes, M., Allaert, F., Sarzi, M., et al. 2014, *MNRAS*, 444, L90
 Bayet, E., Bureau, M., Davis, T. A., et al. 2013, *MNRAS*, 432, 1742
 Bower, R. G., Lucey, J. R., & Ellis, R. S. 1992, *MNRAS*, 254, 601
 Bressan, A., Panuzzo, P., Buson, L., et al. 2006, *ApJ*, 639, L55
 Cappellari, M., Emsellem, E., Krajnović, D., et al. 2011, *MNRAS*, 413, 813
 Cappellari, M., McDermid, R. M., Alatalo, K., et al. 2012, *Nature*, 484, 485
 Cappellari, M., Scott, N., Alatalo, K., et al. 2013, *MNRAS*, 432, 1709
 Combes, F., Young, L. M., & Bureau, M. 2007, *MNRAS*, 377, 1795
 Compiègne, M., Verstraete, L., Jones, A., et al. 2011, *A&A*, 525, A103
 Cowie, L. L., Songaila, A., Hu, E. M., & Cohen, J. G. 1996, *AJ*, 112, 839
 Crocker, A., Krips, M., Bureau, M., et al. 2012, *MNRAS*, 421, 1298
 Crocker, A. F., Bureau, M., Young, L. M., & Combes, F. 2011, *MNRAS*, 410, 1197
 Cutri, R. M., Wright, E. L., Conrow, T., et al. 2013, Explanatory Supplement to the AllWISE Data Release Products, Tech. rep.
 Dale, D. A., Aniano, G., Engelbracht, C. W., et al. 2012, *ApJ*, 745, 95
 Davé, R., Oppenheimer, B. D., & Finlator, K. 2011, *MNRAS*, 415, 11
 Davis, T. A., Alatalo, K., Bureau, M., et al. 2013, *MNRAS*, 429, 534
 Davis, T. A., Alatalo, K., Sarzi, M., et al. 2011, *MNRAS*, 417, 882
 Davis, T. A., Young, L. M., Crocker, A. F., et al. 2014, *MNRAS*, 444, 3427
 de Zeeuw, P. T., Bureau, M., Emsellem, E., et al. 2002, *MNRAS*, 329, 513
 di Serego Alighieri, S., Bianchi, S., Pappalardo, C., et al. 2013, *A&A*, 552, A8
 Doi, Y., Takita, S., Ootsubo, T., et al. 2015, *PASJ*, 67, 50
 Draine, B. T. & Li, A. 2007, *ApJ*, 657, 810
 Draine, B. T. & Salpeter, E. E. 1979, *ApJ*, 231, 77
 Elbaz, D., Daddi, E., Le Borgne, D., et al. 2007, *A&A*, 468, 33
 Emsellem, E., Cappellari, M., Krajnović, D., et al. 2011, *MNRAS*, 414, 888
 Faber, S. M. & Gallagher, J. S. 1976, *ApJ*, 204, 365
 Forman, W., Jones, C., & Tucker, W. 1985, *ApJ*, 293, 102
 Galametz, M., Kennicutt, R. C., Albrecht, M., et al. 2012, *MNRAS*, 425, 763
 Gao, Y. & Solomon, P. M. 2004, *ApJS*, 152, 63
 Goudfrooij, P. & de Jong, T. 1995, *A&A*, 298, 784
 Griffith, R. L., Wright, J. T., Maldonado, J., et al. 2015, *ApJS*, 217, 25
 Guillard, P., Boulanger, F., Lehnert, M. D., et al. 2015, *A&A*, 574, A32
 Gunawardhana, M. L. P., Hopkins, A. M., Sharp, R. G., et al. 2011, *MNRAS*, 415, 1647
 Hao, C.-N., Kennicutt, R. C., Johnson, B. D., et al. 2011, *ApJ*, 741, 124
 Hattori, Y., Kaneda, H., Ishihara, D., et al. 2016, *PASJ*, 68, 37
 Hirashita, H., Nozawa, T., Villaume, A., & Srinivasan, S. 2015, *MNRAS*, 454, 1620
 Hoversten, E. A. & Glazebrook, K. 2008, *ApJ*, 675, 163
 Ishihara, D., Onaka, T., Katata, H., et al. 2010, *A&A*, 514, A1
 Kaneda, H., Ishihara, D., Onaka, T., et al. 2011, *PASJ*, 63, 601
 Kaneda, H., Onaka, T., & Sakon, I. 2005, *ApJ*, 632, L83
 Kaneda, H., Onaka, T., Sakon, I., et al. 2008, *ApJ*, 684, 270
 Kawada, M., Baba, H., Barthel, P. D., et al. 2007, *PASJ*, 59, S389
 Kennicutt, Jr., R. C. 1998, *ApJ*, 498, 541
 Knapp, G. R., Guhathakurta, P., Kim, D.-W., & Jura, M. A. 1989, *ApJS*, 70, 329
 Knapp, G. R. & Rupen, M. P. 1996, *ApJ*, 460, 271
 Knapp, G. R., Turner, E. L., & Cuniffe, P. E. 1985, *AJ*, 90, 454
 Kondo, T., Ishihara, D., Kaneda, H., et al. 2016, *AJ*, 151, 71
 Krajnović, D., Alatalo, K., Blitz, L., et al. 2013a, *MNRAS*, 432, 1768
 Krajnović, D., Emsellem, E., Cappellari, M., et al. 2011, *MNRAS*, 414, 2923
 Krajnović, D., Karick, A. M., Davies, R. L., et al. 2013b, *MNRAS*, 433, 2812
 Lanz, L., Ogle, P. M., Alatalo, K., & Appleton, P. N. 2016, *ApJ*, 826, 29
 Makarov, D., Prugniel, P., Terekhova, N., Courtois, H., & Vauglin, I. 2014, *A&A*, 570, A13
 Malhotra, S., Hollenbach, D., Helou, G., et al. 2000, *ApJ*, 543, 634
 Martig, M., Crocker, A. F., Bournaud, F., et al. 2013, *MNRAS*, 432, 1914
 Martini, P., Dicken, D., & Storch-Bergmann, T. 2013, *ApJ*, 766, 121
 McDermid, R. M., Alatalo, K., Blitz, L., et al. 2015, *MNRAS*, 448, 3484
 McDermid, R. M., Cappellari, M., Alatalo, K., et al. 2014, *ApJ*, 792, L37
 Misiriotis, A., Xilouris, E. M., Papamastorakis, J., Boumis, P., & Goudis, C. D. 2006, *A&A*, 459, 113
 Murakami, H., Baba, H., Barthel, P., et al. 2007, *PASJ*, 59, S369
 Murphy, E. J., Condon, J. J., Schinnerer, E., et al. 2011, *ApJ*, 737, 67
 Nesvadba, N. P. H., Boulanger, F., Lehnert, M. D., Guillard, P., & Salome, P. 2011, *A&A*, 536, L5
 Nyland, K., Alatalo, K., Wrobel, J. M., et al. 2013, *ApJ*, 779, 173
 Nyland, K., Young, L. M., Wrobel, J. M., et al. 2017, *MNRAS*, 464, 1029
 Nyland, K., Young, L. M., Wrobel, J. M., et al. 2016, *MNRAS*, 458, 2221
 Onaka, T., Matsuhara, H., Wada, T., et al. 2007, *PASJ*, 59, S401
 Panuzzo, P., Rampazzo, R., Bressan, A., et al. 2011, *A&A*, 528, A10
 Peeters, E., Spoon, H. W. W., & Tielens, A. G. G. M. 2004, *ApJ*, 613, 986
 Rampazzo, R., Panuzzo, P., Vega, O., et al. 2013, *MNRAS*, 432, 374
 Saintonge, A., Catinella, B., Cortese, L., et al. 2016, *MNRAS*, 462, 1749
 Saintonge, A., Kauffmann, G., Kramer, C., et al. 2011, *MNRAS*, 415, 32
 Schawinski, K., Khochfar, S., Kaviraj, S., et al. 2006, *Nature*, 442, 888
 Scott, N., Cappellari, M., Davies, R. L., et al. 2013, *MNRAS*, 432, 1894
 Serra, P., Oosterloo, T., Morganti, R., et al. 2012, *MNRAS*, 422, 1835
 Shapiro, K. L., Falcón-Barroso, J., van de Ven, G., et al. 2010, *MNRAS*, 402, 2140
 Shipley, H. V., Papovich, C., Rieke, G. H., Brown, M. J. I., & Moustakas, J. 2016, *ApJ*, 818, 60
 Skrutskie, M. F., Cutri, R. M., Stiening, R., et al. 2006, *AJ*, 131, 1163
 Smith, J. D. T., Draine, B. T., Dale, D. A., et al. 2007, *ApJ*, 656, 770
 Smith, M. W. L., Gomez, H. L., Eales, S. A., et al. 2012, *ApJ*, 748, 123
 Suzuki, T., Kaneda, H., Onaka, T., Nakagawa, T., & Shibai, H. 2010, *A&A*, 521, A48
 Takita, S., Doi, Y., Ootsubo, T., et al. 2015, *PASJ*, 67, 51
 Taniguchi, Y. & Ohya, Y. 1998, *ApJ*, 509, L89
 Temi, P., Brighenti, F., & Mathews, W. G. 2007, *ApJ*, 660, 1215
 Temi, P., Brighenti, F., & Mathews, W. G. 2009, *ApJ*, 695, 1
 Temi, P., Mathews, W. G., Brighenti, F., & Bregman, J. D. 2003, *ApJ*, 585, L121
 Thomas, D., Maraston, C., Schawinski, K., Sarzi, M., & Silk, J. 2010, *MNRAS*, 404, 1775
 van Dokkum, P. G. & Conroy, C. 2010, *Nature*, 468, 940
 Wardle, M. & Knapp, G. R. 1986, *AJ*, 91, 23
 Williams, M. J., Bureau, M., & Cappellari, M. 2010, *MNRAS*, 409, 1330
 Yi, S., Demarque, P., & Oemler, Jr., A. 1997, *ApJ*, 486, 201
 Young, L. M., Bureau, M., & Cappellari, M. 2008, *ApJ*, 676, 317
 Young, L. M., Bureau, M., Davis, T. A., et al. 2011, *MNRAS*, 414, 940

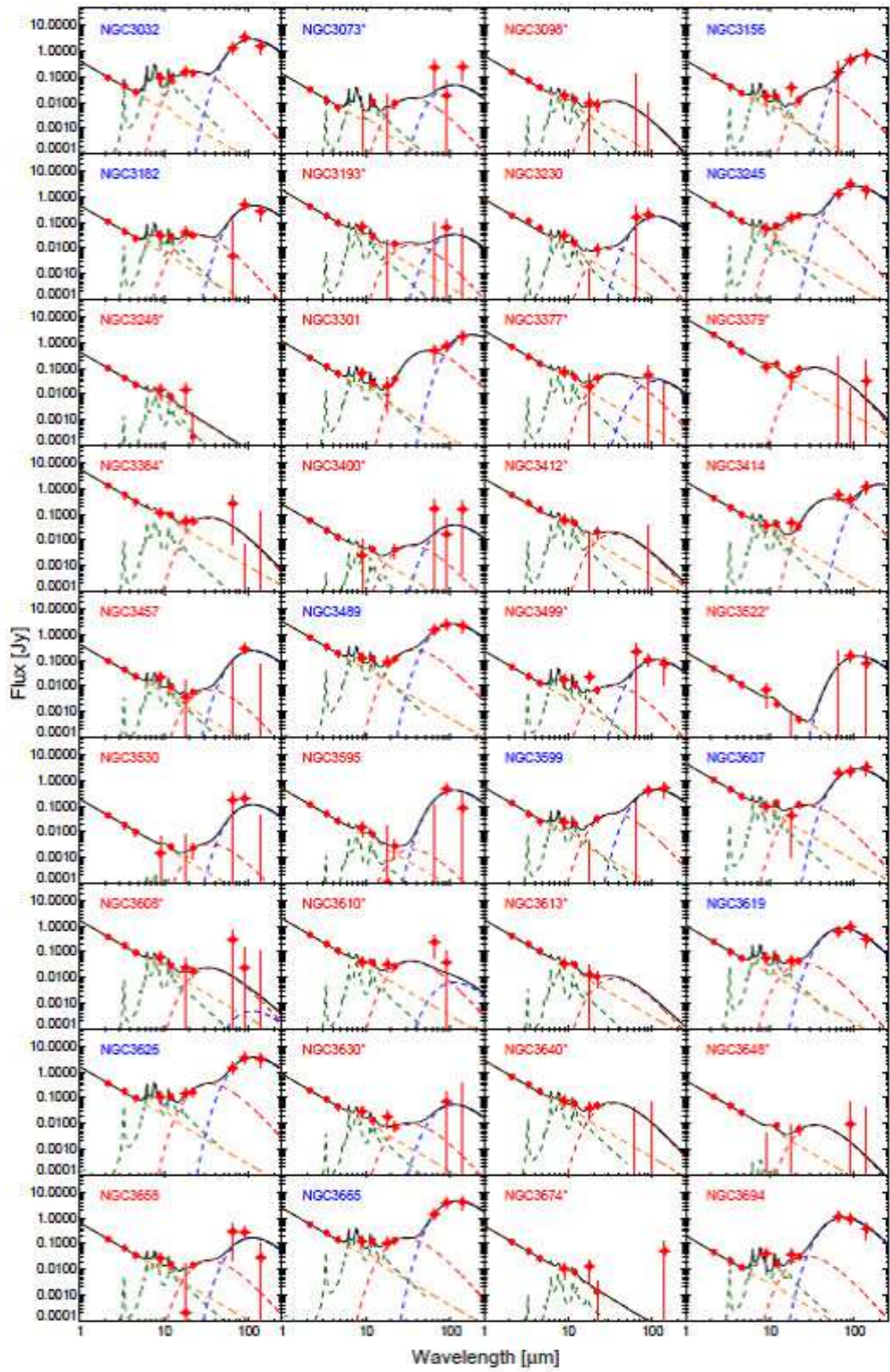


Fig. 3. continued.

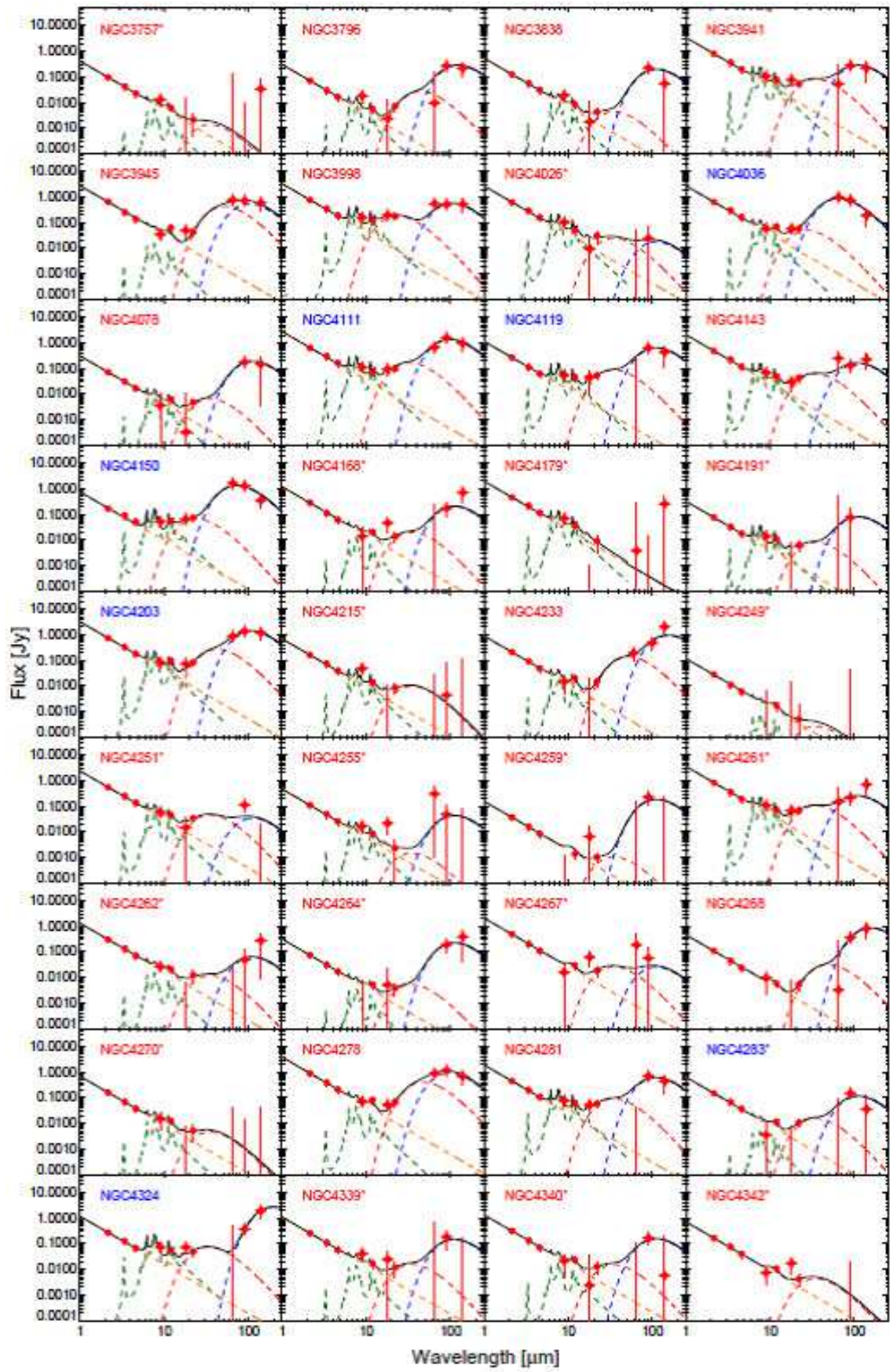


Fig. 3. continued.

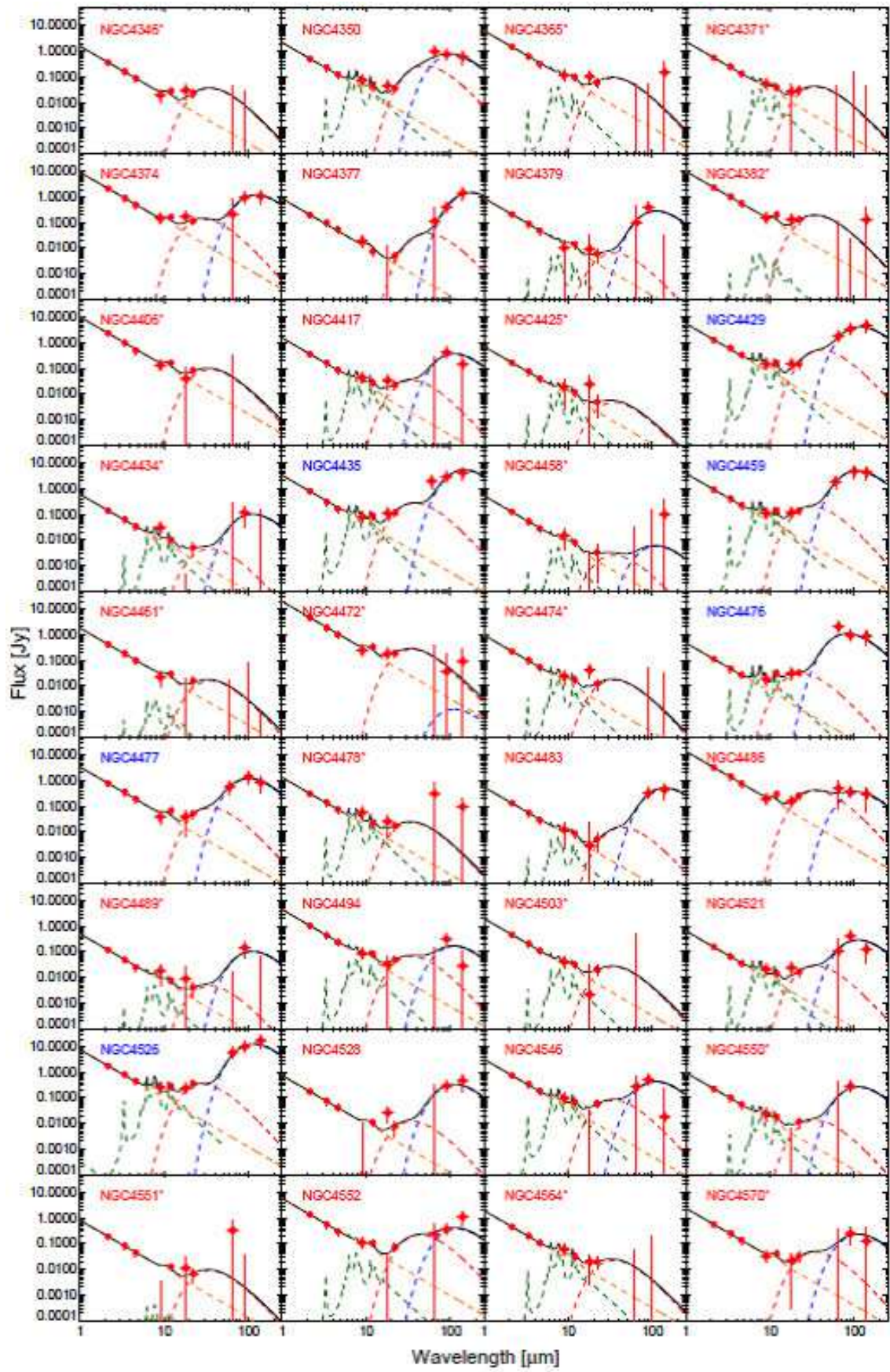


Fig. 3. continued.

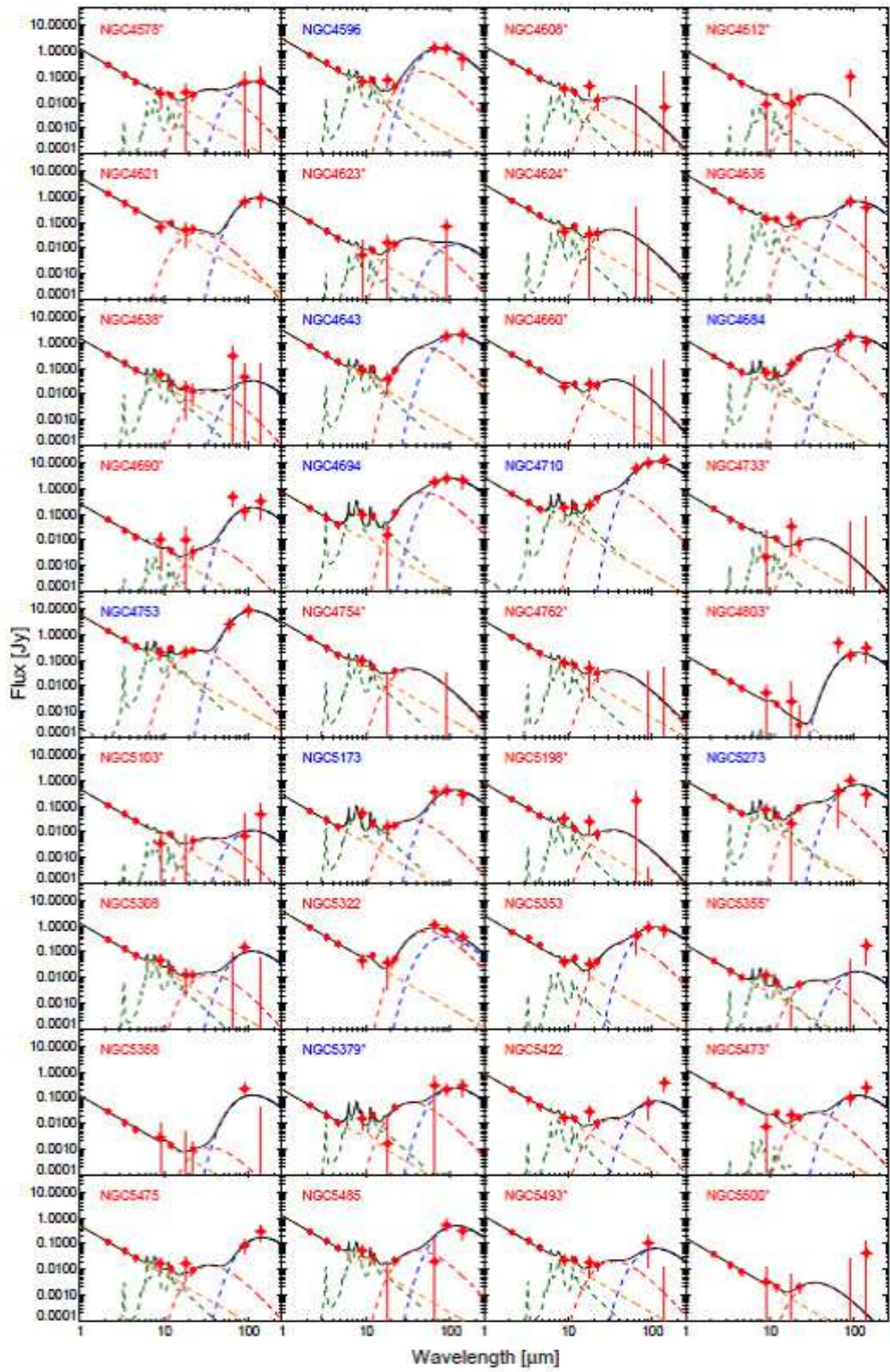


Fig. 3. continued.

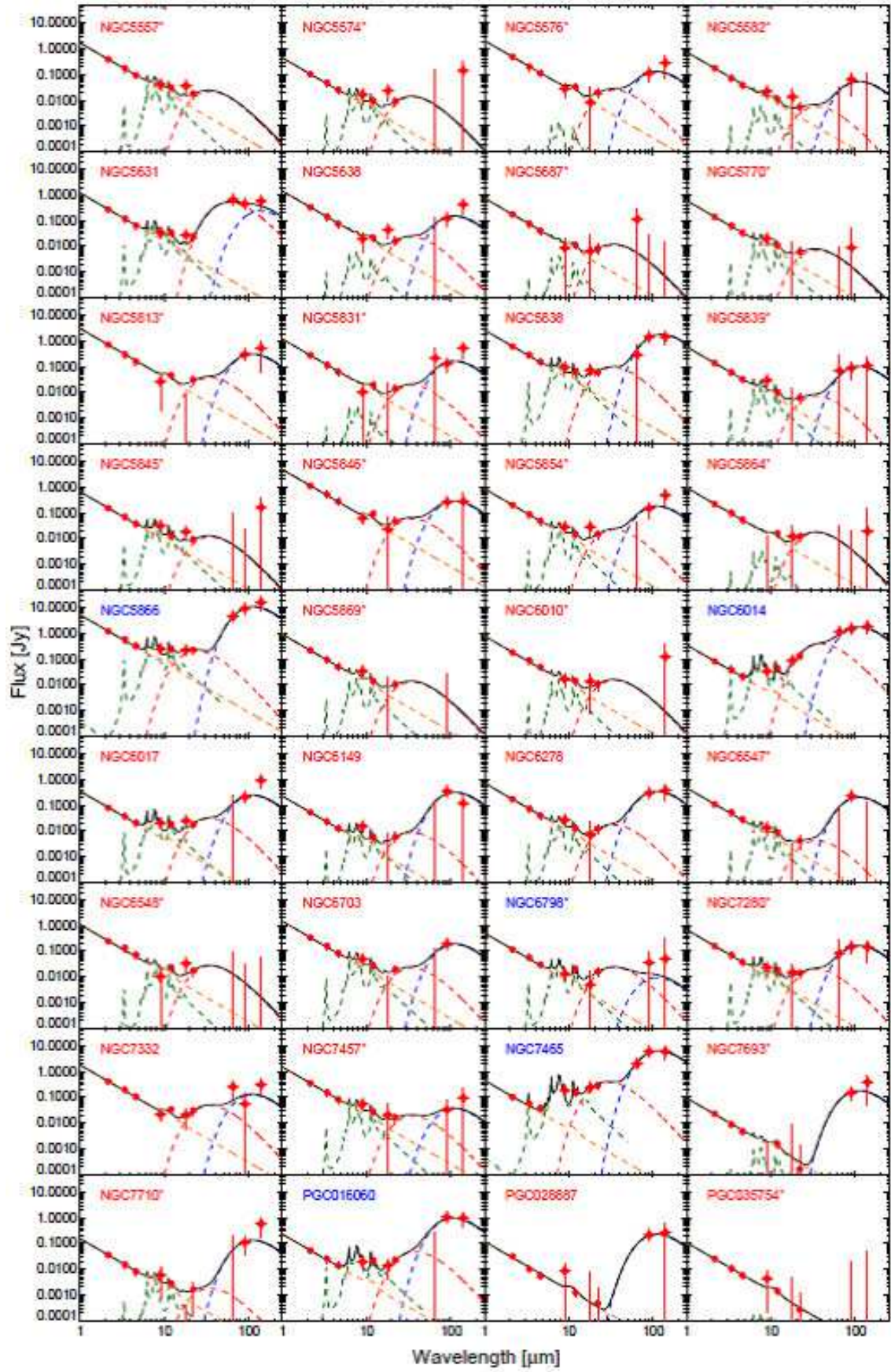


Fig. 3. continued.

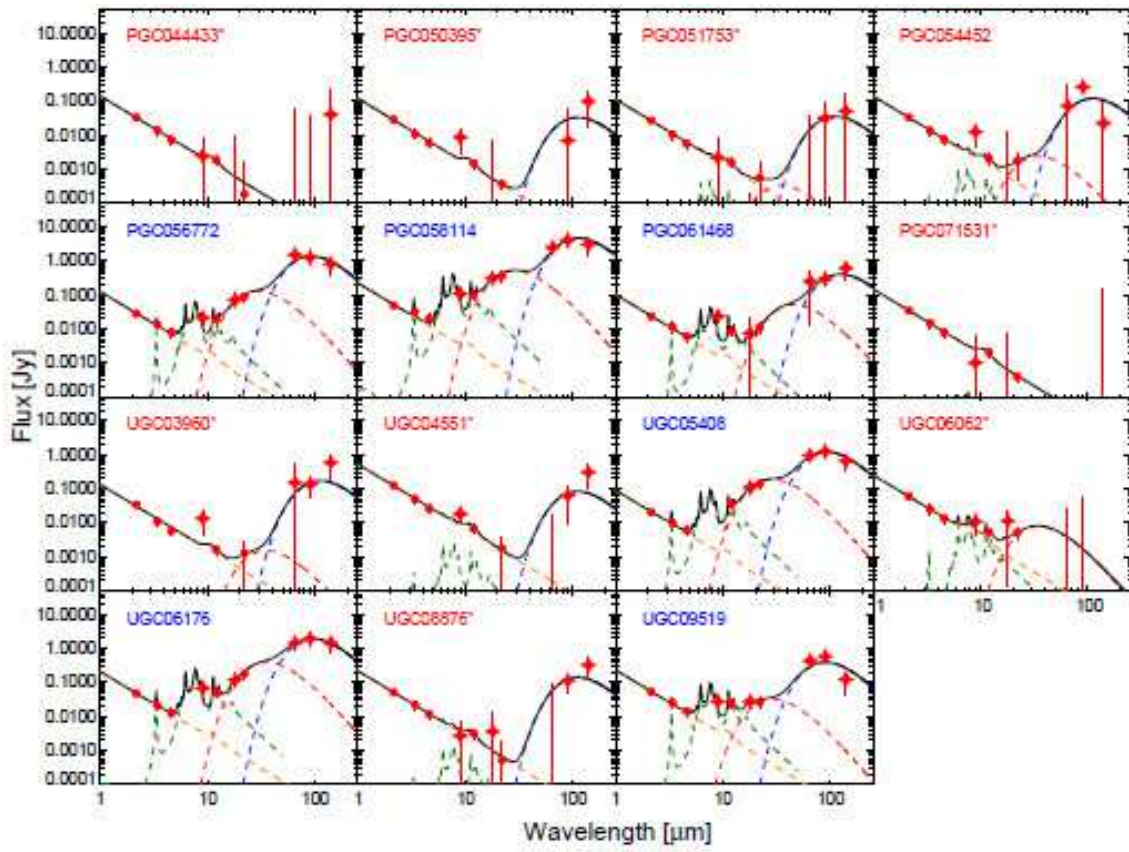


Fig. 3. continued.

**Appendix A: AKARI-measured infrared fluxes of all
ATLAS^{3D} galaxies, and infrared luminosities
derived from SED fitting**

Table A.1. AKARI-measured infrared fluxes of all ATLAS^{3D} galaxies.

Galaxy	9 μm (mJy)	18 μm (mJy)	65 μm (mJy)	90 μm (mJy)	140 μm (mJy)
IC0560	22.09 \pm 7.24	-2.74 \pm 14.81	126.86 \pm 287.93	300.85 \pm 92.04	919.98 \pm 353.35
IC0598	16.27 \pm 5.93	4.54 \pm 10.00	... ^b	239.78 \pm 52.23	201.10 \pm 71.05
IC0676	155.91 \pm 12.00	411.10 \pm 24.43	2258.15 \pm 263.38	3393.55 \pm 63.18	2304.91 \pm 77.22
IC0719	91.47 \pm 7.36	51.06 \pm 11.60	813.76 \pm 252.97	2046.74 \pm 56.34	2123.08 \pm 285.24
IC0782	1.53 \pm 14.34	5.56 \pm 17.69	... ^b	318.52 \pm 60.95	-188.17 \pm 196.01
IC1024	178.18 \pm 6.49	250.94 \pm 13.47	2126.95 \pm 251.55	5800.14 \pm 82.25	7864.90 \pm 183.53
IC3631	2.84 \pm 9.25	-6.92 \pm 14.09	-179.53 \pm 343.00	-24.24 \pm 108.04	-91.55 \pm 75.64
NGC0448	26.17 \pm 5.64	7.05 \pm 11.66	-498.32 \pm 358.69	19.37 \pm 71.52	... ^b
NGC0474	-1.21 \pm 15.88	9.53 \pm 27.07	... ^b	2.84 \pm 110.22	333.20 \pm 252.83
NGC0502	-5.54 \pm 7.61	6.43 \pm 12.95	-88.41 \pm 235.77	10.15 \pm 67.55	... ^b
NGC0509	1.91 \pm 11.29	4.35 \pm 18.11	... ^b	-28.15 \pm 56.44	86.19 \pm 224.23
NGC0516	4.89 \pm 7.87	-1.65 \pm 13.02	-94.96 \pm 350.71	249.47 \pm 76.43	-64.69 \pm 303.49
NGC0524	64.88 \pm 20.75	70.81 \pm 41.79	696.44 \pm 458.18	1851.18 \pm 100.11	3048.60 \pm 352.18
NGC0525	11.56 \pm 9.05	-5.95 \pm 22.19	-305.74 \pm 440.70	-31.31 \pm 95.30	-1062.66 \pm 588.40
NGC0661	7.40 \pm 9.08	9.95 \pm 9.67	-111.75 \pm 304.05	380.90 \pm 80.95	-260.70 \pm 190.48
NGC0680	4.68 \pm 8.38	21.22 \pm 13.66	... ^b	202.88 \pm 82.63	376.06 \pm 220.11
NGC0770	5.20 \pm 7.36	-10.05 \pm 11.09	... ^b	... ^b	... ^b
NGC0821	65.18 \pm 14.52	76.42 \pm 23.71	303.32 \pm 240.86	208.02 \pm 87.63	-257.83 \pm 361.71
NGC0936	55.82 \pm 30.99	-6.19 \pm 51.90	... ^b	435.32 \pm 69.74	-171.50 \pm 137.64
NGC1023	150.16 \pm 24.37	109.60 \pm 45.00	182.60 \pm 250.56	74.13 \pm 64.71	-77.92 \pm 132.30
NGC1121	17.73 \pm 6.05	-16.98 \pm 9.58	177.91 \pm 239.43	3.35 \pm 77.73	... ^b
NGC1222	353.33 \pm 8.04	1064.58 \pm 14.04	11289.63 \pm 344.26	12613.37 \pm 94.35	9493.47 \pm 185.41
NGC1248	19.65 \pm 10.28	18.16 \pm 15.94	-281.98 \pm 221.96	140.14 \pm 80.13	56.11 \pm 176.81
NGC1266	84.42 \pm 10.53	333.47 \pm 18.08	11714.22 \pm 393.10	13428.99 \pm 116.75	11092.29 \pm 308.04
NGC1289	13.39 \pm 8.41	13.35 \pm 24.69	319.36 \pm 305.82	723.11 \pm 90.96	807.54 \pm 192.19
NGC1665	15.13 \pm 18.88	-15.89 \pm 36.33	... ^b	-169.08 \pm 91.80	-134.52 \pm 296.68
NGC2481	11.28 \pm 6.91	28.88 \pm 16.13	... ^b	... ^b	... ^b
NGC2549	60.39 \pm 11.36	33.45 \pm 30.52	... ^b	-13.90 \pm 70.67	-84.19 \pm 253.56
NGC2577	7.55 \pm 10.62	-19.56 \pm 27.88	160.00 \pm 36.00 ^a	1250.00 \pm 193.00 ^a	... ^a
NGC2592	29.13 \pm 17.87	37.73 \pm 24.79	-118.57 \pm 548.53	-67.72 \pm 89.59	-84.68 \pm 296.58
NGC2594	... ^a	-25.05 \pm 13.64	-340.62 \pm 191.10	-95.55 \pm 44.75	-85.23 \pm 171.77
NGC2679	15.89 \pm 11.67	23.98 \pm 27.67	-24.28 \pm 234.12	208.46 \pm 60.79	181.79 \pm 136.02
NGC2685	66.02 \pm 10.20	37.36 \pm 19.71	... ^b	842.64 \pm 42.91	2239.30 \pm 134.75
NGC2695	-0.83 \pm 9.45	26.57 \pm 15.87	... ^b	-272.73 \pm 108.70	155.48 \pm 156.47
NGC2698	44.28 \pm 7.84	-23.48 \pm 10.46	... ^b	367.39 \pm 49.86	... ^b
NGC2699	18.44 \pm 6.91	-3.51 \pm 10.35	79.44 \pm 203.29	71.41 \pm 73.37	54.61 \pm 99.46
NGC2764	227.43 \pm 7.65	301.78 \pm 26.45	2779.17 \pm 238.58	5762.03 \pm 64.86	6479.78 \pm 288.04
NGC2768	67.96 \pm 48.13	48.16 \pm 59.93	472.80 \pm 565.93	458.41 \pm 103.67	747.48 \pm 420.77
NGC2778	20.26 \pm 8.38	16.18 \pm 16.24	-337.31 \pm 147.70	456.60 \pm 71.52	244.53 \pm 115.49
NGC2824	40.39 \pm 6.58	64.77 \pm 10.75	630.64 \pm 309.26	1564.48 \pm 52.88	1016.50 \pm 152.58
NGC2852	-4.30 \pm 6.51	2.34 \pm 9.45	-211.10 \pm 210.08	33.60 \pm 53.46	... ^b
NGC2859	69.67 \pm 11.30	4.21 \pm 20.47	468.12 \pm 226.05	660.07 \pm 54.60	363.20 \pm 142.21
NGC2880	34.21 \pm 13.46	39.99 \pm 32.41	91.33 \pm 329.26	192.11 \pm 55.95	450.83 \pm 117.29
NGC2950	58.73 \pm 10.41	-1.27 \pm 15.37	6.39 \pm 204.51	82.08 \pm 39.25	158.41 \pm 86.79
NGC2962	11.63 \pm 13.54	38.78 \pm 20.52	150.09 \pm 296.85	495.39 \pm 64.40	1671.71 \pm 212.41
NGC2974	98.46 \pm 25.19	65.77 \pm 37.19	365.99 \pm 330.64	1083.13 \pm 80.70	2380.69 \pm 222.63
NGC3032	89.03 \pm 12.02	158.63 \pm 15.81	1310.93 \pm 306.98	3533.09 \pm 76.29	1583.76 \pm 82.02
NGC3073	-7.47 \pm 15.59	-4.61 \pm 23.95	234.57 \pm 196.62	18.41 \pm 52.96	242.43 \pm 121.60
NGC3098	18.79 \pm 6.83	9.31 \pm 16.04	-128.39 \pm 265.95	-64.67 \pm 72.51	-386.44 \pm 223.06
NGC3156	17.76 \pm 10.31	37.45 \pm 20.08	150.44 \pm 267.86	446.58 \pm 75.94	736.41 \pm 184.56
NGC3182	31.22 \pm 8.40	41.56 \pm 16.77	4.97 \pm 150.11	508.17 \pm 45.96	278.92 \pm 77.41
NGC3193	69.13 \pm 15.99	-3.75 \pm 22.51	-142.28 \pm 232.99	64.48 \pm 69.28	-102.89 \pm 156.10
NGC3226	41.28 \pm 18.34	2.05 \pm 23.65	... ^b	... ^b	... ^b
NGC3230	31.58 \pm 11.21	-16.50 \pm 17.92	161.04 \pm 279.60	205.44 \pm 54.95	-212.26 \pm 144.72
NGC3245	60.19 \pm 13.59	153.32 \pm 22.68	1307.80 \pm 233.28	3225.60 \pm 66.75	1824.74 \pm 142.60
NGC3248	14.60 \pm 8.83	14.54 \pm 12.84	-356.26 \pm 282.41	-86.67 \pm 58.23	-255.13 \pm 185.92
NGC3301	66.18 \pm 12.31	21.17 \pm 19.14	497.52 \pm 323.36	758.28 \pm 79.16	1807.68 \pm 242.41
NGC3377	74.52 \pm 17.41	19.81 \pm 41.84	... ^b	55.47 \pm 69.56	-351.97 \pm 335.52

Table A.1. continued.

Galaxy	9 μm (mJy)	18 μm (mJy)	65 μm (mJy)	90 μm (mJy)	140 μm (mJy)
NGC3379	113.38 ± 22.02	48.33 ± 33.40	-20.99 ± 295.23	-27.63 ± 43.46	32.41 ± 181.01
NGC3384	112.17 ± 19.28	53.66 ± 31.71	262.24 ± 249.95	-56.07 ± 61.97	-17.58 ± 150.51
NGC3400	2.48 ± 8.57	-19.03 ± 14.43	165.24 ± 188.75	16.50 ± 51.20	157.89 ± 136.21
NGC3412	60.58 ± 16.48	-8.37 ± 26.00	...	-43.08 ± 77.34	-299.67 ± 166.45
NGC3414	36.54 ± 14.76	46.61 ± 22.24	577.72 ± 246.21	377.99 ± 65.90	1207.45 ± 132.40
NGC3457	21.76 ± 6.84	3.63 ± 12.42	-242.21 ± 316.92	282.71 ± 58.22	-113.19 ± 175.75
NGC3458	12.22 ± 8.80	-24.54 ± 11.20	...	-164.63 ± 61.82	46.80 ± 75.84
NGC3489	120.94 ± 12.63	86.75 ± 21.76	1524.15 ± 300.91	2476.44 ± 51.32	2195.04 ± 110.13
NGC3499	17.24 ± 6.26	22.20 ± 9.40	214.99 ± 235.54	102.62 ± 39.49	71.53 ± 48.39
NGC3522	6.86 ± 5.46	-16.27 ± 17.15	-66.55 ± 304.41	149.33 ± 65.13	75.15 ± 121.77
NGC3530	1.46 ± 4.78	-1.54 ± 8.85	171.01 ± 173.75	199.24 ± 41.54	-17.45 ± 60.28
NGC3595	14.99 ± 8.34	0.10 ± 16.07	-302.25 ± 409.48	461.52 ± 70.59	83.62 ± 224.39
NGC3599	23.76 ± 11.24	-29.18 ± 32.74	-212.26 ± 349.25	407.69 ± 83.84	507.72 ± 185.78
NGC3605	13.94 ± 9.77	7.36 ± 18.25
NGC3607	96.58 ± 28.11	42.52 ± 41.27	1970.03 ± 319.66	2275.15 ± 93.75	3305.25 ± 173.40
NGC3608	62.63 ± 17.24	24.39 ± 31.76	304.65 ± 415.53	24.04 ± 116.47	-162.39 ± 263.76
NGC3610	40.04 ± 9.17	32.40 ± 15.23	241.53 ± 178.56	38.58 ± 73.09	-329.93 ± 137.04
NGC3613	34.39 ± 10.93	12.75 ± 17.66	-75.51 ± 56.81
NGC3619	57.08 ± 13.16	44.70 ± 23.90	621.67 ± 208.89	954.24 ± 45.99	319.44 ± 45.81
NGC3626	106.73 ± 13.16	148.10 ± 21.51	1427.62 ± 322.23	3614.93 ± 76.39	3305.24 ± 195.69
NGC3630	29.33 ± 6.13	18.21 ± 11.69	-486.17 ± 385.52	70.68 ± 94.08	-274.36 ± 649.14
NGC3640	75.91 ± 15.79	39.58 ± 24.68	0.00 ± 39.00 ^a	0.00 ± 66.00 ^a	...
NGC3641	12.59 ± 7.15	-7.33 ± 8.33	0.00 ± 41.00 ^a	0.00 ± 145.00 ^a	...
NGC3648	-2.12 ± 6.12	-2.77 ± 11.50	-248.98 ± 228.09	9.24 ± 55.83	-51.43 ± 92.10
NGC3658	26.84 ± 9.49	0.20 ± 17.33	299.10 ± 270.26	276.90 ± 64.64	28.78 ± 81.13
NGC3665	123.14 ± 15.34	105.40 ± 27.61	1424.53 ± 269.55	3911.87 ± 53.88	4241.70 ± 101.93
NGC3674	10.61 ± 6.83	12.90 ± 10.26	...	-60.53 ± 47.78	51.25 ± 67.70
NGC3694	41.11 ± 13.05	37.53 ± 21.00	1136.62 ± 239.63	922.90 ± 64.88	386.33 ± 139.64
NGC3757	12.77 ± 5.86	-0.20 ± 14.62	-85.81 ± 220.38	-48.15 ± 57.15	33.19 ± 47.02
NGC3796	17.76 ± 8.00	2.28 ± 11.15	9.40 ± 145.26	267.71 ± 54.24	213.67 ± 44.29
NGC3838	18.92 ± 7.00	1.72 ± 9.53	...	221.68 ± 44.10	53.72 ± 96.65
NGC3941	104.77 ± 16.53	75.55 ± 25.82	52.30 ± 253.93	275.63 ± 51.25	217.30 ± 109.59
NGC3945	34.83 ± 15.61	49.96 ± 25.73	759.65 ± 210.88	727.79 ± 48.57	602.26 ± 87.67
NGC3998	158.19 ± 11.07	196.59 ± 19.10	540.99 ± 186.84	511.96 ± 43.29	529.14 ± 71.10
NGC4026	102.73 ± 10.62	9.56 ± 16.61	-242.10 ± 289.05	24.24 ± 41.85	...
NGC4036	58.67 ± 13.46	58.43 ± 22.67	990.20 ± 219.56	751.14 ± 47.57	192.19 ± 73.94
NGC4078	3.59 ± 6.69	0.32 ± 10.74	...	177.87 ± 57.43	146.94 ± 123.39
NGC4111	110.46 ± 7.43	95.14 ± 12.43	666.39 ± 227.45	1596.75 ± 69.31	952.24 ± 101.19
NGC4119	55.19 ± 23.24	46.25 ± 35.54	-89.93 ± 325.33	640.81 ± 60.49	433.68 ± 229.21
NGC4143	68.25 ± 11.27	29.97 ± 16.41	249.16 ± 177.77	131.20 ± 52.08	227.92 ± 65.53
NGC4150	51.67 ± 7.87	65.44 ± 14.26	1651.55 ± 215.16	1306.65 ± 38.94	348.75 ± 51.03
NGC4168	14.07 ± 15.14	45.68 ± 25.48	-153.50 ± 394.43	172.51 ± 79.93	714.11 ± 238.30
NGC4179	68.80 ± 9.65	-23.01 ± 23.87	3.80 ± 292.46	-76.40 ± 90.45	254.45 ± 286.58
NGC4191	13.93 ± 8.99	-7.07 ± 14.53	-361.04 ± 874.08	75.75 ± 98.01	...
NGC4203	82.20 ± 18.86	72.01 ± 34.46	849.43 ± 263.92	1346.32 ± 46.51	1185.25 ± 73.59
NGC4215	47.60 ± 11.47	-7.70 ± 18.29	-212.73 ± 235.30	4.29 ± 79.54	-100.01 ± 210.00
NGC4233	14.41 ± 9.43	-0.20 ± 18.41	190.00 ± 37.00 ^a	480.00 ± 87.00 ^a	2031.16 ± 258.93
NGC4249	-1.34 ± 8.28	-0.09 ± 15.29	...	-10.57 ± 50.61	-246.35 ± 113.73
NGC4251	57.91 ± 9.93	14.37 ± 20.35	...	111.36 ± 50.32	-35.38 ± 50.96
NGC4255	16.49 ± 7.15	21.46 ± 14.15	300.85 ± 293.77	47.75 ± 63.10	-144.40 ± 206.25
NGC4259	-5.37 ± 6.45	6.47 ± 9.92	-169.37 ± 307.51	224.63 ± 112.37	-0.17 ± 235.95
NGC4261	105.98 ± 21.02	66.78 ± 35.63	149.26 ± 394.04	214.36 ± 92.00	696.73 ± 274.96
NGC4262	26.97 ± 7.38	-6.45 ± 12.48	-323.77 ± 344.51	49.32 ± 73.96	278.66 ± 230.65
NGC4264	-1.36 ± 8.91	5.19 ± 17.40	...	190.78 ± 83.39	387.30 ± 281.79
NGC4267	16.00 ± 17.83	63.01 ± 34.64	186.13 ± 327.11	57.24 ± 89.03	-293.79 ± 233.19
NGC4268	9.83 ± 7.42	-14.31 ± 22.14	3.26 ± 274.87	363.61 ± 80.23	820.50 ± 260.35
NGC4270	15.56 ± 9.50	-12.06 ± 19.92	-196.08 ± 233.06	-55.59 ± 69.06	-99.62 ± 130.95
NGC4278	70.88 ± 12.78	53.70 ± 22.41	901.94 ± 185.60	1180.53 ± 54.73	687.50 ± 70.36
NGC4281	77.37 ± 12.64	52.99 ± 22.06	-238.97 ± 278.86	710.34 ± 94.55	438.75 ± 178.24

Table A.1. continued.

Galaxy	9 μm (mJy)	18 μm (mJy)	65 μm (mJy)	90 μm (mJy)	140 μm (mJy)
NGC4283	3.52 \pm 8.11	-12.98 \pm 20.40	-97.64 \pm 191.36	149.70 \pm 57.12	35.86 \pm 88.89
NGC4324	72.98 \pm 14.69	72.39 \pm 23.69	-134.19 \pm 602.68	371.28 \pm 58.70	1939.36 \pm 133.50
NGC4339	40.70 \pm 17.95	24.42 \pm 26.30	-100.17 \pm 744.13	184.35 \pm 125.31	-140.08 \pm 304.58
NGC4340	20.93 \pm 16.19	2.36 \pm 33.60	-177.61 \pm 288.69	167.86 \pm 62.21	5.75 \pm 183.17
NGC4342	7.35 \pm 4.99	17.11 \pm 10.11	... ^b	-39.71 \pm 59.18	... ^b
NGC4346	19.07 \pm 9.05	29.31 \pm 15.51	-208.59 \pm 251.51	-39.95 \pm 66.84	... ^b
NGC4350	73.49 \pm 8.96	44.28 \pm 14.84	967.73 \pm 257.05	753.42 \pm 52.67	599.41 \pm 125.48
NGC4365	114.88 \pm 26.07	102.10 \pm 41.72	-390.38 \pm 438.28	-40.15 \pm 95.48	147.96 \pm 205.72
NGC4371	53.24 \pm 19.77	26.15 \pm 27.33	0.00 \pm 47.00 ^a	0.00 \pm 157.00 ^a	-252.57 \pm 268.50
NGC4374	146.18 \pm 26.27	172.25 \pm 57.86	210.71 \pm 664.13	957.68 \pm 118.95	1084.09 \pm 203.62
NGC4377	18.92 \pm 7.69	-5.00 \pm 17.09	112.96 \pm 273.77	400.21 \pm 57.06	1423.95 \pm 209.50
NGC4379	10.42 \pm 10.33	9.21 \pm 23.47	100.12 \pm 361.98	390.55 \pm 89.13	-177.04 \pm 192.01
NGC4382	152.32 \pm 36.25	131.49 \pm 65.11	-402.94 \pm 516.92	-95.19 \pm 115.62	129.85 \pm 241.12
NGC4387	29.46 \pm 8.34	-13.23 \pm 18.30	-116.42 \pm 343.65	188.58 \pm 69.54	-325.22 \pm 216.54
NGC4406	133.30 \pm 42.59	40.16 \pm 66.70	-424.73 \pm 766.37	-175.19 \pm 146.50	... ^b
NGC4417	43.59 \pm 10.84	34.10 \pm 19.74	-4.33 \pm 277.55	429.78 \pm 82.38	147.98 \pm 174.78
NGC4425	19.34 \pm 16.63	24.06 \pm 25.21	-493.04 \pm 399.97	-220.22 \pm 122.66	-862.69 \pm 327.92
NGC4429	152.51 \pm 23.54	151.71 \pm 34.28	1873.01 \pm 562.37	3467.62 \pm 111.38	4773.09 \pm 220.32
NGC4434	30.14 \pm 8.20	-18.71 \pm 19.08	-38.95 \pm 325.27	117.37 \pm 81.72	-65.32 \pm 216.26
NGC4435	80.42 \pm 25.76	110.38 \pm 37.37	1990.00 \pm 43.00 ^a	2903.77 \pm 113.81	4137.15 \pm 238.08
NGC4442	51.98 \pm 14.46	10.77 \pm 27.39	-615.07 \pm 439.86	-91.50 \pm 72.05	-572.90 \pm 232.99
NGC4452	21.14 \pm 11.25	17.00 \pm 16.46	-581.27 \pm 390.31	... ^b	-140.65 \pm 122.96
NGC4458	14.87 \pm 10.52	-14.78 \pm 18.09	0.00 \pm 34.00 ^a	0.00 \pm 142.00 ^a	100.27 \pm 260.47
NGC4459	113.03 \pm 22.75	117.21 \pm 28.83	1870.00 \pm 66.00 ^a	4820.00 \pm 134.00 ^a	4383.07 \pm 348.11
NGC4461	21.91 \pm 12.97	-3.00 \pm 24.00	0.00 \pm 17.00 ^a	0.00 \pm 85.00 ^a	-446.59 \pm 388.00
NGC4472	241.91 \pm 41.93	179.83 \pm 73.48	-55.87 \pm 412.51	35.78 \pm 135.63	90.24 \pm 191.68
NGC4473	91.54 \pm 13.83	-2.54 \pm 25.28	... ^b	-299.87 \pm 177.94	... ^b
NGC4474	23.85 \pm 12.70	41.36 \pm 21.55	... ^b	-15.77 \pm 64.22	-142.11 \pm 159.17
NGC4476	18.18 \pm 8.20	30.69 \pm 14.33	2078.80 \pm 539.68	946.12 \pm 108.40	884.13 \pm 173.16
NGC4477	37.97 \pm 19.35	38.76 \pm 32.30	570.00 \pm 51.00 ^a	1410.00 \pm 98.00 ^a	838.00 \pm 311.98
NGC4478	56.41 \pm 10.11	25.25 \pm 19.65	302.94 \pm 546.84	-163.28 \pm 150.33	93.09 \pm 114.23
NGC4483	12.21 \pm 10.00	2.83 \pm 19.27	-533.86 \pm 302.18	322.09 \pm 68.73	431.49 \pm 135.87
NGC4486	188.94 \pm 34.92	152.94 \pm 55.81	493.03 \pm 402.78	363.37 \pm 97.78	295.53 \pm 184.34
NGC4486A	29.46 \pm 6.85	-0.33 \pm 12.95	-139.45 \pm 200.96	133.35 \pm 57.10	-189.41 \pm 108.78
NGC4489	18.20 \pm 13.29	8.89 \pm 19.40	-408.35 \pm 418.32	147.47 \pm 88.68	-158.61 \pm 210.81
NGC4494	86.94 \pm 22.23	32.36 \pm 37.42	-149.45 \pm 285.98	320.01 \pm 66.84	28.49 \pm 84.76
NGC4503	41.26 \pm 19.02	2.15 \pm 29.03	-18.45 \pm 558.24	-207.32 \pm 199.74	... ^b
NGC4521	21.24 \pm 6.93	24.03 \pm 11.14	107.26 \pm 210.10	422.05 \pm 48.64	126.09 \pm 65.61
NGC4526	257.98 \pm 22.98	236.26 \pm 34.27	5831.36 \pm 651.64	9830.22 \pm 142.13	17367.27 \pm 220.50
NGC4528	0.09 \pm 10.83	26.26 \pm 15.10	-110.81 \pm 411.30	287.82 \pm 81.49	469.53 \pm 186.81
NGC4546	96.69 \pm 12.58	-1.18 \pm 38.78	279.24 \pm 377.19	517.45 \pm 82.54	17.78 \pm 226.18
NGC4550	24.06 \pm 11.67	-8.78 \pm 15.37	-81.48 \pm 511.47	282.87 \pm 96.03	-996.11 \pm 401.41
NGC4551	-14.20 \pm 17.31	11.15 \pm 18.29	329.39 \pm 512.85	-74.65 \pm 108.47	... ^b
NGC4552	107.71 \pm 17.95	-0.02 \pm 41.01	232.93 \pm 336.62	367.38 \pm 66.98	1109.74 \pm 197.04
NGC4564	60.57 \pm 12.41	19.63 \pm 16.98	0.00 \pm 60.00 ^a	0.00 \pm 190.00 ^a	-475.01 \pm 170.92
NGC4570	31.96 \pm 12.45	21.90 \pm 21.53	-184.23 \pm 528.79	250.29 \pm 157.37	126.29 \pm 323.66
NGC4578	21.93 \pm 15.68	24.57 \pm 27.69	... ^b	59.41 \pm 88.71	64.02 \pm 172.67
NGC4596	63.86 \pm 21.78	74.77 \pm 33.61	1339.50 \pm 414.85	1277.59 \pm 95.16	506.42 \pm 204.10
NGC4608	34.09 \pm 15.10	43.23 \pm 24.55	-235.42 \pm 277.04	-144.02 \pm 70.34	6.48 \pm 145.94
NGC4612	8.32 \pm 15.14	8.76 \pm 21.77	... ^b	100.31 \pm 80.09	-80.61 \pm 59.69
NGC4621	64.90 \pm 27.12	50.73 \pm 39.48	... ^b	646.07 \pm 97.82	926.39 \pm 227.38
NGC4623	5.40 \pm 13.56	16.28 \pm 16.23	... ^b	70.46 \pm 69.80	-180.20 \pm 101.99
NGC4624	44.06 \pm 24.17	35.60 \pm 37.87	-106.55 \pm 488.77	-100.16 \pm 113.49	-300.26 \pm 239.78
NGC4636	141.18 \pm 44.90	160.18 \pm 72.60	-732.77 \pm 692.54	669.91 \pm 137.24	394.31 \pm 567.50
NGC4638	58.60 \pm 8.79	17.46 \pm 16.28	308.55 \pm 446.42	46.39 \pm 114.28	-15.83 \pm 157.12
NGC4643	86.87 \pm 14.37	39.39 \pm 28.22	... ^b	1843.36 \pm 72.84	2156.65 \pm 230.65
NGC4649	186.90 \pm 34.04	40.08 \pm 53.25	... ^b	... ^b	... ^b
NGC4660	19.31 \pm 8.89	24.94 \pm 13.17	0.00 \pm 48.00 ^a	0.00 \pm 101.00 ^a	-49.98 \pm 250.14
NGC4684	68.80 \pm 14.16	142.39 \pm 24.65	852.64 \pm 416.86	1859.01 \pm 89.08	1107.51 \pm 286.47

Table A.1. continued.

Galaxy	9 μm (mJy)	18 μm (mJy)	65 μm (mJy)	90 μm (mJy)	140 μm (mJy)
NGC4690	10.19 \pm 9.54	10.04 \pm 20.83	485.11 \pm 257.94	136.39 \pm 70.08	322.18 \pm 206.45
NGC4694	99.02 \pm 18.29	15.58 \pm 22.89	1820.17 \pm 384.20	2533.78 \pm 67.90	2177.04 \pm 304.40
NGC4697	88.96 \pm 32.32	106.54 \pm 50.51	460.00 \pm 23.00 ^a	1240.00 \pm 76.00 ^a	... ^a
NGC4710	182.15 \pm 15.42	231.89 \pm 25.86	6201.75 \pm 424.24	9966.46 \pm 111.55	13399.18 \pm 166.79
NGC4733	2.18 \pm 20.37	33.22 \pm 30.51	... ^b	-0.67 \pm 54.49	-40.62 \pm 121.26
NGC4753	203.52 \pm 26.76	207.74 \pm 55.62	2570.00 \pm 59.00 ^a	9010.00 \pm 199.00 ^a	... ^a
NGC4754	95.93 \pm 19.27	-2.14 \pm 32.75	... ^b	-31.45 \pm 62.43	... ^b
NGC4762	78.81 \pm 29.44	47.94 \pm 43.99	... ^b	-39.04 \pm 74.47	-67.60 \pm 114.70
NGC4803	5.36 \pm 5.56	2.39 \pm 11.07	478.41 \pm 252.15	154.26 \pm 51.59	300.41 \pm 163.57
NGC5103	3.47 \pm 7.63	-13.38 \pm 21.17	-247.56 \pm 161.41	6.83 \pm 41.27	48.20 \pm 72.68
NGC5173	52.33 \pm 12.76	15.42 \pm 10.61	354.56 \pm 233.77	394.61 \pm 50.30	275.97 \pm 94.04
NGC5198	33.05 \pm 11.55	24.53 \pm 17.27	161.88 \pm 219.07	-56.73 \pm 55.97	-136.02 \pm 84.69
NGC5273	73.00 \pm 23.46	20.74 \pm 33.49	378.69 \pm 355.52	995.61 \pm 72.55	285.04 \pm 138.58
NGC5308	47.24 \pm 7.89	12.72 \pm 10.76	-48.60 \pm 135.83	150.77 \pm 42.65	-21.90 \pm 81.27
NGC5322	46.06 \pm 21.59	37.92 \pm 34.19	1140.44 \pm 232.14	692.98 \pm 50.26	388.85 \pm 84.81
NGC5342	7.68 \pm 4.86	0.02 \pm 10.10	-50.72 \pm 151.49	-80.12 \pm 65.28	... ^b
NGC5353	40.17 \pm 11.97	33.71 \pm 21.09	434.73 \pm 349.67	898.18 \pm 76.47	734.66 \pm 106.89
NGC5355	12.21 \pm 6.62	-21.36 \pm 22.15	... ^b	-6.63 \pm 55.01	174.74 \pm 116.72
NGC5358	2.82 \pm 7.67	-9.05 \pm 13.51	... ^b	224.50 \pm 59.60	-44.54 \pm 85.97
NGC5379	15.28 \pm 9.59	1.62 \pm 17.18	301.90 \pm 407.09	208.95 \pm 73.91	294.10 \pm 127.16
NGC5422	16.62 \pm 8.12	28.72 \pm 16.12	-288.41 \pm 191.45	60.69 \pm 44.72	390.89 \pm 90.10
NGC5473	7.35 \pm 11.50	21.20 \pm 14.44	... ^b	99.94 \pm 46.76	250.44 \pm 92.66
NGC5475	16.62 \pm 8.49	16.58 \pm 12.57	-197.43 \pm 120.18	83.20 \pm 39.95	302.00 \pm 80.72
NGC5481	23.64 \pm 11.53	7.11 \pm 15.38	... ^b	... ^b	... ^b
NGC5485	52.86 \pm 13.13	-7.30 \pm 25.52	20.03 \pm 191.84	532.89 \pm 45.33	314.45 \pm 58.25
NGC5493	22.71 \pm 8.18	18.27 \pm 13.11	... ^b	106.42 \pm 91.99	-219.93 \pm 204.90
NGC5500	3.18 \pm 8.75	-7.24 \pm 14.02	... ^b	-7.92 \pm 32.22	42.82 \pm 72.80
NGC5507	26.96 \pm 8.02	-35.56 \pm 19.09	... ^b	-61.91 \pm 52.65	... ^b
NGC5557	41.09 \pm 17.19	36.40 \pm 20.46	... ^b	-51.54 \pm 36.16	-88.11 \pm 32.44
NGC5574	16.48 \pm 10.05	23.60 \pm 14.12	-54.16 \pm 205.81	-131.17 \pm 60.17	142.58 \pm 154.36
NGC5576	27.99 \pm 14.05	8.18 \pm 21.79	-277.59 \pm 257.24	114.46 \pm 55.48	284.84 \pm 162.34
NGC5582	22.45 \pm 11.44	13.43 \pm 15.49	-182.72 \pm 210.41	63.70 \pm 46.92	-12.90 \pm 119.25
NGC5611	-14.97 \pm 6.31	-0.04 \pm 9.48	125.85 \pm 161.71	69.57 \pm 40.86	75.65 \pm 58.20
NGC5631	34.83 \pm 9.27	27.41 \pm 14.23	664.72 \pm 157.96	450.02 \pm 44.79	583.97 \pm 90.38
NGC5638	19.56 \pm 14.02	43.75 \pm 23.75	-119.06 \pm 243.23	123.18 \pm 60.60	425.75 \pm 112.82
NGC5687	8.58 \pm 11.42	6.48 \pm 19.53	112.92 \pm 188.29	-36.27 \pm 63.11	-78.68 \pm 84.16
NGC5770	20.06 \pm 9.83	-1.42 \pm 16.23	-216.51 \pm 220.83	8.83 \pm 42.14	-167.82 \pm 81.32
NGC5813	26.36 \pm 24.20	-38.93 \pm 46.55	-341.86 \pm 292.25	303.15 \pm 105.28	527.34 \pm 391.56
NGC5831	10.24 \pm 12.77	-0.70 \pm 23.52	216.68 \pm 284.05	130.87 \pm 61.23	534.75 \pm 180.20
NGC5838	94.72 \pm 14.23	74.35 \pm 21.71	286.10 \pm 396.65	1456.09 \pm 57.23	1454.12 \pm 150.54
NGC5839	29.55 \pm 9.96	-0.24 \pm 15.49	70.09 \pm 212.18	89.23 \pm 52.56	110.80 \pm 131.97
NGC5845	31.72 \pm 4.92	18.33 \pm 9.29	-105.88 \pm 193.96	-35.86 \pm 58.01	162.42 \pm 209.18
NGC5846	61.83 \pm 24.82	22.87 \pm 41.81	... ^b	263.42 \pm 101.10	279.20 \pm 281.01
NGC5854	28.23 \pm 10.67	28.17 \pm 17.92	-280.27 \pm 321.48	150.61 \pm 83.17	487.45 \pm 166.18
NGC5864	-1.53 \pm 13.82	12.23 \pm 19.73	-255.83 \pm 284.09	-71.18 \pm 89.99	19.17 \pm 133.75
NGC5866	247.44 \pm 15.23	220.79 \pm 18.70	4573.14 \pm 231.09	9188.32 \pm 63.58	16097.43 \pm 97.72
NGC5869	33.70 \pm 9.36	-1.64 \pm 20.76	... ^b	-26.85 \pm 55.05	-530.31 \pm 276.70
NGC6010	16.40 \pm 8.08	13.35 \pm 12.59	-498.45 \pm 310.18	-126.90 \pm 72.46	121.03 \pm 234.77
NGC6014	32.86 \pm 11.84	86.45 \pm 21.39	1150.65 \pm 214.66	1510.87 \pm 55.20	1860.82 \pm 131.97
NGC6017	20.01 \pm 5.73	24.47 \pm 8.95	-1.68 \pm 257.38	205.26 \pm 74.45	923.82 \pm 166.59
NGC6149	14.93 \pm 5.97	-9.64 \pm 16.95	-19.44 \pm 173.33	348.69 \pm 49.72	117.30 \pm 143.58
NGC6278	26.75 \pm 9.29	6.97 \pm 15.92	... ^b	297.77 \pm 53.72	377.40 \pm 126.89
NGC6547	13.14 \pm 6.92	-18.76 \pm 21.64	-241.07 \pm 301.53	228.20 \pm 76.26	-152.64 \pm 261.41
NGC6548	10.23 \pm 13.42	32.97 \pm 20.56	-61.13 \pm 154.50	-46.67 \pm 78.66	-162.35 \pm 206.26
NGC6703	49.16 \pm 8.75	-6.75 \pm 16.33	-31.14 \pm 161.19	193.97 \pm 52.73	-840.04 \pm 469.52
NGC6798	13.11 \pm 6.40	4.92 \pm 11.57	-187.04 \pm 109.85	35.84 \pm 57.60	50.47 \pm 281.29
NGC7280	23.13 \pm 12.90	15.20 \pm 17.56	82.76 \pm 190.65	149.60 \pm 64.97	144.04 \pm 81.36
NGC7332	21.68 \pm 10.26	20.75 \pm 14.83	257.81 \pm 152.79	55.37 \pm 82.16	310.47 \pm 74.44
NGC7454	0.82 \pm 13.10	3.82 \pm 23.14	... ^b	97.14 \pm 57.51	66.64 \pm 176.45

Table A.1. continued.

Galaxy	9 μm (mJy)	18 μm (mJy)	65 μm (mJy)	90 μm (mJy)	140 μm (mJy)
NGC7457	54.97 \pm 18.49	20.51 \pm 32.74	-245.86 \pm 236.09	32.91 \pm 45.43	94.83 \pm 121.33
NGC7465	184.93 \pm 6.03	243.18 \pm 9.17	2076.94 \pm 196.93	6169.73 \pm 65.99	6094.62 \pm 194.56
NGC7693	-5.90 \pm 7.65	-13.63 \pm 22.58	... ^b	151.03 \pm 63.74	387.38 \pm 278.60
NGC7710	5.85 \pm 5.12	-11.45 \pm 11.78	-74.10 \pm 283.14	108.80 \pm 68.36	580.37 \pm 281.26
PGC016060	19.29 \pm 9.17	13.90 \pm 9.93	-55.66 \pm 308.03	1064.04 \pm 69.06	982.56 \pm 248.02
PGC028887	8.56 \pm 8.68	-8.96 \pm 15.90	-332.74 \pm 265.98	213.40 \pm 56.91	264.66 \pm 253.68
PGC029321	63.74 \pm 5.01	227.68 \pm 10.09	1083.73 \pm 307.99	1097.12 \pm 65.28	1156.41 \pm 238.88
PGC035754	4.19 \pm 3.95	-6.10 \pm 10.61	... ^b	-20.85 \pm 41.12	-33.91 \pm 79.34
PGC042549	-2.21 \pm 7.01	-29.53 \pm 24.42	... ^a	... ^a	... ^a
PGC044433	2.41 \pm 6.00	-1.38 \pm 10.35	-236.57 \pm 292.85	-37.56 \pm 73.37	39.97 \pm 190.85
PGC050395	8.44 \pm 5.40	-4.19 \pm 11.49	... ^b	6.84 \pm 45.90	97.04 \pm 64.02
PGC051753	2.14 \pm 5.70	-9.57 \pm 9.72	-208.24 \pm 240.44	30.94 \pm 61.57	49.97 \pm 100.88
PGC054452	12.23 \pm 7.99	-0.34 \pm 12.43	71.71 \pm 216.15	255.98 \pm 63.11	22.32 \pm 59.05
PGC056772	21.14 \pm 7.11	71.15 \pm 9.05	1489.64 \pm 246.96	1246.73 \pm 58.33	804.77 \pm 190.37
PGC058114	106.79 \pm 8.09	305.10 \pm 10.59	2455.07 \pm 229.21	4007.11 \pm 64.68	2999.71 \pm 258.96
PGC061468	23.62 \pm 6.70	7.49 \pm 14.56	249.49 \pm 230.55	292.99 \pm 56.56	607.21 \pm 184.07
PGC071531	1.01 \pm 5.40	-0.38 \pm 8.13	-331.86 \pm 230.12	-87.59 \pm 77.01	-100.15 \pm 245.86
PGC170172	-18.63 \pm 9.12	-6.40 \pm 14.42	-391.44 \pm 392.59	-174.39 \pm 100.36	-122.34 \pm 249.03
UGC03960	13.43 \pm 9.07	-17.13 \pm 15.85	150.69 \pm 355.43	134.69 \pm 73.76	585.08 \pm 287.11
UGC04551	18.19 \pm 7.09	-20.98 \pm 15.97	-216.83 \pm 229.21	63.44 \pm 53.40	302.48 \pm 136.38
UGC05408	... ^a	108.44 \pm 11.86	957.89 \pm 233.95	1244.20 \pm 50.19	656.04 \pm 89.95
UGC06062	10.90 \pm 6.59	11.28 \pm 11.08	-282.66 \pm 305.20	-1.47 \pm 58.69	-419.98 \pm 151.66
UGC06176	68.53 \pm 6.14	118.46 \pm 10.68	1462.14 \pm 368.35	1947.63 \pm 76.50	1454.00 \pm 169.94
UGC08876	2.75 \pm 4.84	3.65 \pm 10.24	-141.39 \pm 231.93	113.92 \pm 58.65	328.51 \pm 125.43
UGC09519	27.78 \pm 5.87	28.14 \pm 7.75	438.62 \pm 169.53	583.64 \pm 29.93	124.76 \pm 47.40

(a)

Not observed with AKARI. When possible, the missing 65 and/or 90 μm flux densities are replaced by IRAS 60 and/or 100 μm measurements from NED.

(b) Measurement likely affected by source confusion or instrumental artefact.

Table A.2. IR luminosities derived from SED fitting.

Galaxy	L_{PAH} (10^{41} erg s $^{-1}$)	L_{warm} (10^{41} erg s $^{-1}$)	L_{cold} (10^{41} erg s $^{-1}$)
IC0560	2.88 ± 1.09	2.53 ± 0.96	9.77 ± 3.31
IC0598	1.79 ± 1.09	1.82 ± 0.78	11.94 ± 3.22
IC0676	44.56 ± 5.63	91.41 ± 10.81	77.84 ± 13.03
IC0719	32.99 ± 4.25	14.69 ± 4.17	71.24 ± 12.51
IC0782	0.11 ± 0.41	0.26 ± 0.50	13.65 ± 4.53
IC1024	48.60 ± 5.25	32.64 ± 4.10	152.36 ± 22.71
IC3631	1.07 ± 0.80	1.40 ± 0.85	0.00 ± 5.04
NGC0448	2.81 ± 1.30	0.52 ± 0.59	0.34 ± 2.61
NGC0474	0.00 ± 2.26	1.25 ± 0.78	1.58 ± 4.16
NGC0502	0.00 ± 0.78	0.25 ± 0.27	0.33 ± 3.63
NGC0509	0.86 ± 0.63	1.16 ± 0.53	0.00 ± 2.42
NGC0516	0.74 ± 0.72	0.13 ± 0.44	11.01 ± 4.40
NGC0524	3.33 ± 4.89	9.06 ± 3.41	47.74 ± 9.13
NGC0525	0.00 ± 0.32	0.49 ± 0.30	0.00 ± 3.74
NGC0661	1.38 ± 1.61	0.85 ± 0.64	9.69 ± 3.89
NGC0680	0.00 ± 2.76	2.57 ± 1.02	12.75 ± 5.19
NGC1023	0.00 ± 1.60	2.60 ± 0.95	0.07 ± 0.31
NGC1222	192.07 ± 19.37	462.57 ± 48.06	640.00 ± 96.96
NGC1248	1.27 ± 1.18	0.99 ± 0.60	4.08 ± 2.94
NGC1266	34.99 ± 5.64	181.48 ± 20.38	556.85 ± 81.44
NGC1289	2.27 ± 2.02	1.42 ± 0.91	45.43 ± 9.67
NGC1665	0.73 ± 1.88	0.31 ± 1.01	0.00 ± 5.51
NGC2549	1.40 ± 0.64	0.82 ± 0.36	0.00 ± 0.43
NGC2577	2.17 ± 2.17	10.39 ± 3.91	88.74 ± 48.77
NGC2592	1.04 ± 1.12	0.67 ± 0.44	0.00 ± 2.27
NGC2679	0.58 ± 1.07	1.87 ± 0.80	7.97 ± 2.71
NGC2685	6.53 ± 1.50	18.54 ± 5.32	17.85 ± 8.35
NGC2699	1.43 ± 1.01	0.39 ± 0.31	1.92 ± 1.73
NGC2764	155.91 ± 17.86	82.82 ± 12.23	389.60 ± 55.73
NGC2768	3.76 ± 5.73	3.80 ± 1.87	9.32 ± 2.67
NGC2824	22.89 ± 5.22	17.47 ± 3.42	98.87 ± 17.90
NGC2852	0.00 ± 0.49	0.30 ± 0.27	0.89 ± 1.83
NGC2859	8.46 ± 3.18	1.71 ± 1.20	18.21 ± 3.62
NGC2880	0.83 ± 1.05	0.35 ± 0.39	5.55 ± 1.67
NGC2950	1.91 ± 0.95	1.00 ± 0.55	0.72 ± 0.35
NGC2962	4.26 ± 3.80	11.42 ± 4.79	51.00 ± 12.27
NGC3032	15.85 ± 3.19	12.66 ± 1.88	51.51 ± 8.61
NGC3073	4.56 ± 1.85	1.83 ± 0.71	1.87 ± 2.28
NGC3098	1.31 ± 0.97	0.69 ± 0.52	0.00 ± 1.58
NGC3156	2.68 ± 1.13	1.75 ± 0.74	10.41 ± 2.52
NGC3182	11.51 ± 3.83	6.10 ± 1.84	18.99 ± 4.21
NGC3193	6.95 ± 4.70	1.77 ± 1.44	1.36 ± 2.96
NGC3230	6.10 ± 4.09	1.93 ± 1.62	10.64 ± 4.46
NGC3245	4.10 ± 2.71	13.16 ± 2.21	45.16 ± 7.16
NGC3248	0.69 ± 0.74	0.00 ± 0.23	0.00 ± 1.49
NGC3301	6.12 ± 1.99	19.89 ± 6.36	24.82 ± 8.33
NGC3377	0.79 ± 0.72	0.85 ± 0.40	0.14 ± 0.35
NGC3379	0.00 ± 1.18	1.27 ± 0.67	0.00 ± 0.20
NGC3384	0.91 ± 1.17	1.06 ± 0.56	0.00 ± 0.31
NGC3400	0.26 ± 0.43	0.43 ± 0.30	0.86 ± 1.24
NGC3412	0.88 ± 0.71	0.25 ± 0.28	0.00 ± 0.37
NGC3414	4.04 ± 3.11	20.00 ± 5.84	18.04 ± 9.00
NGC3457	1.16 ± 0.57	0.33 ± 0.20	3.54 ± 1.25
NGC3489	4.59 ± 1.10	3.80 ± 1.05	14.13 ± 2.31
NGC3499	3.59 ± 1.14	0.82 ± 0.35	2.69 ± 1.05
NGC3522	0.00 ± 0.23	0.00 ± 0.02	3.52 ± 1.70
NGC3530	0.03 ± 0.42	0.38 ± 0.31	4.07 ± 1.70
NGC3595	1.13 ± 1.50	0.29 ± 0.49	18.66 ± 5.20
NGC3599	2.56 ± 1.13	2.31 ± 0.88	6.44 ± 1.79

Table A.2. continued.

Galaxy	L_{PAH} (10^{41} erg s $^{-1}$)	L_{warm} (10^{41} erg s $^{-1}$)	L_{cold} (10^{41} erg s $^{-1}$)
NGC3607	7.84 ± 6.23	7.17 ± 2.75	53.58 ± 8.47
NGC3608	3.27 ± 2.14	1.29 ± 0.85	0.01 ± 2.23
NGC3610	1.87 ± 1.74	2.17 ± 0.83	0.10 ± 1.25
NGC3613	2.35 ± 3.16	0.86 ± 1.19	0.00 ± 2.29
NGC3619	14.26 ± 4.30	4.39 ± 1.67	35.23 ± 6.26
NGC3626	15.81 ± 2.97	16.34 ± 3.05	52.54 ± 8.79
NGC3630	1.98 ± 1.18	0.68 ± 0.47	1.26 ± 2.46
NGC3640	8.56 ± 4.57	5.05 ± 2.34	0.00 ± 1.60
NGC3648	0.04 ± 1.31	0.99 ± 0.58	0.00 ± 2.05
NGC3658	4.90 ± 2.47	2.69 ± 1.18	6.75 ± 2.64
NGC3665	45.06 ± 9.88	24.41 ± 6.35	177.61 ± 27.85
NGC3674	0.87 ± 1.35	0.00 ± 0.47	0.00 ± 1.91
NGC3694	9.91 ± 3.25	5.69 ± 2.04	71.68 ± 11.96
NGC3757	0.32 ± 0.49	0.08 ± 0.19	0.00 ± 0.81
NGC3796	0.55 ± 0.46	1.30 ± 0.55	4.88 ± 1.32
NGC3838	0.69 ± 0.72	0.29 ± 0.25	4.03 ± 1.23
NGC3941	2.86 ± 1.09	1.35 ± 0.51	1.46 ± 0.40
NGC3945	0.98 ± 3.45	18.40 ± 6.56	11.99 ± 3.72
NGC3998	7.85 ± 1.70	6.10 ± 0.96	4.25 ± 0.80
NGC4026	3.21 ± 0.97	0.52 ± 0.47	0.12 ± 0.31
NGC4036	4.87 ± 3.82	4.54 ± 1.73	33.86 ± 5.79
NGC4078	1.55 ± 1.50	1.13 ± 0.70	10.43 ± 3.73
NGC4111	6.16 ± 1.27	4.57 ± 0.91	12.08 ± 2.19
NGC4119	4.48 ± 1.74	2.84 ± 1.03	6.40 ± 1.46
NGC4143	3.31 ± 1.23	1.77 ± 0.68	1.43 ± 0.54
NGC4150	3.27 ± 0.78	2.05 ± 0.47	13.65 ± 2.10
NGC4168	1.35 ± 2.93	2.28 ± 1.33	7.39 ± 3.41
NGC4179	3.05 ± 1.14	0.00 ± 0.37	0.00 ± 1.00
NGC4191	5.54 ± 2.60	1.46 ± 0.87	4.62 ± 6.40
NGC4203	4.05 ± 1.88	5.74 ± 1.97	11.37 ± 2.14
NGC4215	3.64 ± 2.02	1.14 ± 0.86	0.00 ± 3.08
NGC4233	3.21 ± 3.12	12.77 ± 5.08	28.74 ± 12.63
NGC4249	0.16 ± 0.54	0.05 ± 0.42	0.00 ± 3.05
NGC4251	2.88 ± 1.68	1.97 ± 0.92	0.46 ± 0.59
NGC4255	1.53 ± 1.25	0.17 ± 0.49	1.55 ± 2.50
NGC4259	0.00 ± 0.35	0.17 ± 0.10	9.49 ± 6.18
NGC4261	16.39 ± 7.92	11.78 ± 4.44	8.63 ± 3.93
NGC4262	0.43 ± 0.63	0.34 ± 0.32	0.56 ± 0.71
NGC4264	0.62 ± 1.25	0.88 ± 0.58	12.00 ± 5.24
NGC4267	0.00 ± 1.10	0.79 ± 0.47	0.24 ± 0.89
NGC4268	0.00 ± 0.96	2.75 ± 1.82	23.01 ± 6.40
NGC4270	2.10 ± 2.35	0.68 ± 0.96	0.00 ± 3.23
NGC4278	1.33 ± 1.59	8.69 ± 3.03	9.89 ± 2.19
NGC4281	12.35 ± 3.56	6.60 ± 2.32	13.80 ± 3.55
NGC4283	0.14 ± 0.42	0.44 ± 0.20	1.01 ± 0.51
NGC4324	6.65 ± 1.67	2.49 ± 0.82	15.54 ± 3.66
NGC4339	0.42 ± 0.68	0.48 ± 0.39	1.41 ± 1.29
NGC4340	0.78 ± 1.21	0.61 ± 0.48	1.96 ± 0.93
NGC4342	0.00 ± 0.40	0.14 ± 0.11	0.00 ± 0.68
NGC4346	0.00 ± 0.64	0.81 ± 0.32	0.00 ± 0.54
NGC4350	3.64 ± 1.10	5.37 ± 1.99	6.65 ± 1.51
NGC4365	2.65 ± 5.80	5.65 ± 2.57	0.00 ± 2.00
NGC4371	1.17 ± 1.55	1.37 ± 0.69	0.00 ± 1.15
NGC4374	0.00 ± 4.59	6.49 ± 2.15	13.86 ± 3.04
NGC4377	0.00 ± 0.38	0.93 ± 0.69	11.17 ± 2.63
NGC4379	0.16 ± 0.54	0.19 ± 0.19	2.65 ± 1.07
NGC4382	0.28 ± 5.50	7.17 ± 2.95	0.00 ± 1.44
NGC4406	0.00 ± 4.98	3.07 ± 1.86	0.00 ± 1.79
NGC4417	1.38 ± 0.93	1.05 ± 0.47	3.58 ± 1.07
NGC4425	0.38 ± 0.53	0.15 ± 0.22	0.00 ± 1.44

Table A.2. continued.

Galaxy	L_{PAH} (10^{41} erg s $^{-1}$)	L_{warm} (10^{41} erg s $^{-1}$)	L_{cold} (10^{41} erg s $^{-1}$)
NGC4429	8.96 ± 3.41	14.43 ± 4.10	40.25 ± 7.28
NGC4434	1.11 ± 0.79	0.27 ± 0.30	1.90 ± 1.66
NGC4435	4.85 ± 2.81	8.51 ± 2.49	42.64 ± 8.13
NGC4458	0.16 ± 0.35	0.08 ± 0.18	0.06 ± 0.85
NGC4459	7.08 ± 2.93	6.84 ± 1.74	49.73 ± 14.73
NGC4461	0.10 ± 1.08	0.50 ± 0.38	0.00 ± 0.50
NGC4472	0.00 ± 6.54	9.14 ± 3.79	0.01 ± 1.38
NGC4474	0.69 ± 0.65	0.49 ± 0.26	0.00 ± 0.62
NGC4476	1.96 ± 1.06	1.68 ± 0.49	17.02 ± 3.22
NGC4477	0.00 ± 2.02	2.68 ± 1.06	13.30 ± 4.33
NGC4478	1.71 ± 0.87	0.77 ± 0.42	0.00 ± 1.16
NGC4483	0.22 ± 0.39	0.38 ± 0.41	4.17 ± 1.15
NGC4486	0.00 ± 5.49	14.13 ± 4.31	3.48 ± 1.37
NGC4489	0.14 ± 0.30	0.13 ± 0.13	0.92 ± 0.86
NGC4494	2.08 ± 2.54	2.20 ± 1.03	1.71 ± 0.73
NGC4503	0.80 ± 1.30	0.83 ± 0.50	0.00 ± 2.30
NGC4521	5.78 ± 3.21	5.27 ± 1.89	17.11 ± 4.35
NGC4526	17.10 ± 4.43	13.40 ± 2.64	124.33 ± 18.35
NGC4528	0.00 ± 0.46	0.36 ± 0.25	3.12 ± 0.99
NGC4546	3.25 ± 1.22	1.79 ± 0.79	2.98 ± 0.89
NGC4550	0.71 ± 0.65	0.38 ± 0.28	2.40 ± 1.10
NGC4551	0.01 ± 0.53	0.27 ± 0.22	0.00 ± 1.19
NGC4552	1.27 ± 2.26	5.23 ± 2.53	3.29 ± 1.14
NGC4564	1.74 ± 1.06	0.67 ± 0.48	0.00 ± 1.19
NGC4570	0.00 ± 1.38	1.63 ± 0.87	2.52 ± 1.80
NGC4578	0.40 ± 0.81	0.98 ± 0.55	0.61 ± 0.89
NGC4596	3.55 ± 2.34	3.96 ± 2.21	18.67 ± 3.62
NGC4608	0.76 ± 1.01	0.45 ± 0.44	0.00 ± 0.77
NGC4612	0.26 ± 0.77	0.67 ± 0.36	0.00 ± 0.63
NGC4621	0.00 ± 2.40	1.51 ± 0.73	6.64 ± 1.53
NGC4623	0.26 ± 0.41	0.88 ± 0.39	0.15 ± 0.80
NGC4624	1.68 ± 2.41	1.64 ± 1.11	0.00 ± 1.22
NGC4636	2.29 ± 3.28	3.67 ± 1.60	4.98 ± 1.56
NGC4638	2.45 ± 1.02	0.46 ± 0.59	0.36 ± 1.19
NGC4643	5.09 ± 2.04	14.83 ± 5.52	18.26 ± 4.32
NGC4660	0.00 ± 0.70	0.95 ± 0.36	0.00 ± 0.70
NGC4684	3.69 ± 1.05	11.26 ± 2.08	10.83 ± 2.24
NGC4690	0.43 ± 1.06	0.96 ± 0.68	11.07 ± 4.87
NGC4694	10.91 ± 2.22	16.53 ± 6.01	25.37 ± 5.26
NGC4710	18.91 ± 3.10	26.39 ± 4.21	120.70 ± 17.64
NGC4733	0.16 ± 0.38	0.27 ± 0.18	0.00 ± 0.44
NGC4753	27.18 ± 8.51	19.43 ± 4.91	167.56 ± 60.22
NGC4754	2.95 ± 1.77	1.34 ± 0.81	0.00 ± 0.69
NGC4762	4.87 ± 4.46	2.18 ± 1.86	0.00 ± 1.37
NGC4803	0.05 ± 0.52	0.00 ± 0.42	11.29 ± 3.77
NGC5103	0.30 ± 0.67	0.33 ± 0.31	0.22 ± 0.83
NGC5173	17.11 ± 4.42	4.73 ± 1.81	22.94 ± 5.00
NGC5198	3.32 ± 3.11	2.00 ± 1.20	0.00 ± 3.31
NGC5273	4.61 ± 1.58	4.24 ± 1.46	6.54 ± 1.55
NGC5308	5.87 ± 2.80	1.58 ± 1.27	3.89 ± 1.82
NGC5322	0.00 ± 7.58	45.42 ± 15.54	17.11 ± 7.98
NGC5353	2.28 ± 6.65	24.23 ± 9.08	40.04 ± 9.01
NGC5355	3.14 ± 1.40	1.23 ± 0.59	0.84 ± 2.98
NGC5358	0.00 ± 0.36	0.19 ± 0.30	6.83 ± 3.46
NGC5379	7.41 ± 2.62	6.87 ± 2.42	8.08 ± 2.94
NGC5422	1.49 ± 2.07	1.68 ± 0.87	2.56 ± 1.80
NGC5473	0.30 ± 3.81	3.35 ± 1.38	5.06 ± 2.24
NGC5475	2.08 ± 1.37	1.35 ± 0.59	4.05 ± 1.75
NGC5485	6.88 ± 2.71	3.36 ± 1.63	11.03 ± 2.44
NGC5493	4.20 ± 4.41	3.66 ± 1.77	3.54 ± 5.54

Table A.2. continued.

Galaxy	L_{PAH} (10^{41} erg s $^{-1}$)	L_{warm} (10^{41} erg s $^{-1}$)	L_{cold} (10^{41} erg s $^{-1}$)
NGC5500	0.00 ± 0.36	0.34 ± 0.20	0.00 ± 1.25
NGC5557	8.30 ± 6.82	3.89 ± 2.23	0.00 ± 1.96
NGC5574	1.19 ± 0.82	0.87 ± 0.38	0.00 ± 1.37
NGC5576	0.11 ± 2.73	1.83 ± 0.99	2.93 ± 1.49
NGC5582	0.61 ± 1.31	0.51 ± 0.39	1.52 ± 1.45
NGC5631	6.55 ± 2.75	26.90 ± 7.77	5.22 ± 4.59
NGC5638	0.54 ± 2.14	1.80 ± 0.86	3.66 ± 1.73
NGC5687	0.37 ± 1.34	0.98 ± 0.55	0.00 ± 1.62
NGC5770	0.64 ± 0.59	0.29 ± 0.21	0.00 ± 0.57
NGC5813	0.00 ± 6.44	4.40 ± 2.42	11.24 ± 4.77
NGC5831	0.26 ± 2.04	1.57 ± 0.76	4.30 ± 1.90
NGC5838	9.80 ± 3.18	5.55 ± 1.75	28.46 ± 5.48
NGC5839	0.97 ± 0.78	0.42 ± 0.27	1.86 ± 1.05
NGC5845	3.22 ± 1.11	0.88 ± 0.42	0.00 ± 1.63
NGC5846	0.00 ± 5.83	4.16 ± 2.15	6.22 ± 2.64
NGC5854	1.94 ± 1.59	1.82 ± 0.77	4.68 ± 2.43
NGC5864	0.35 ± 2.10	1.69 ± 0.85	0.00 ± 2.64
NGC5866	16.42 ± 3.10	7.99 ± 1.28	89.87 ± 12.55
NGC5869	1.35 ± 1.30	0.94 ± 0.52	0.00 ± 1.43
NGC6010	1.71 ± 1.91	1.65 ± 0.94	0.00 ± 2.87
NGC6014	21.27 ± 6.08	54.19 ± 11.78	82.08 ± 14.54
NGC6017	5.90 ± 1.76	3.05 ± 0.98	7.56 ± 2.93
NGC6149	2.40 ± 1.25	1.39 ± 0.77	16.22 ± 4.27
NGC6278	4.58 ± 3.59	3.69 ± 1.64	23.46 ± 5.85
NGC6547	2.50 ± 2.25	0.82 ± 0.87	12.49 ± 5.86
NGC6548	1.33 ± 1.71	1.60 ± 0.74	0.00 ± 1.54
NGC6703	4.57 ± 2.21	1.75 ± 1.01	4.75 ± 1.81
NGC6798	6.42 ± 3.33	3.95 ± 1.58	0.49 ± 3.28
NGC7280	3.01 ± 1.60	1.35 ± 0.66	3.41 ± 1.40
NGC7332	0.00 ± 1.96	2.86 ± 1.08	2.38 ± 1.54
NGC7457	0.95 ± 0.68	0.37 ± 0.26	0.22 ± 0.30
NGC7465	73.39 ± 7.89	48.16 ± 5.84	195.90 ± 28.98
NGC7693	0.16 ± 0.35	0.00 ± 0.32	8.48 ± 3.64
NGC7710	0.54 ± 0.54	0.24 ± 0.37	5.78 ± 3.41
PGC016060	13.20 ± 4.09	7.41 ± 2.60	54.90 ± 11.85
PGC028887	0.00 ± 0.38	0.00 ± 0.49	14.38 ± 4.85
PGC035754	0.04 ± 0.37	0.00 ± 0.30	0.00 ± 2.35
PGC044433	0.01 ± 0.50	0.00 ± 0.52	0.00 ± 4.63
PGC050395	0.00 ± 0.35	0.01 ± 0.04	1.69 ± 2.32
PGC051753	0.08 ± 0.40	0.06 ± 0.31	1.90 ± 3.26
PGC054452	0.12 ± 0.30	0.24 ± 0.23	3.83 ± 1.75
PGC056772	11.26 ± 3.96	28.14 ± 4.33	94.24 ± 15.23
PGC058114	27.13 ± 3.58	42.06 ± 4.58	96.42 ± 14.43
PGC061468	6.47 ± 1.74	6.21 ± 2.28	17.11 ± 4.58
PGC071531	0.02 ± 0.27	0.00 ± 0.03	0.00 ± 2.90
UGC03960	0.00 ± 0.33	0.20 ± 0.33	7.05 ± 3.56
UGC04551	0.24 ± 0.84	0.00 ± 0.36	2.42 ± 1.74
UGC05408	23.70 ± 13.01	57.23 ± 8.30	110.84 ± 18.68
UGC06062	1.92 ± 1.33	1.38 ± 0.70	0.00 ± 3.59
UGC06176	49.25 ± 6.57	75.38 ± 10.55	132.13 ± 23.06
UGC08876	0.20 ± 0.61	0.00 ± 0.33	6.08 ± 2.89
UGC09519	8.69 ± 1.96	3.54 ± 0.94	13.75 ± 2.78